Showcasing research from Professor Sunghwan Lee's Laboratory of Thin Film Materials and Devices, School of Engineering Technology, Purdue University, West Lafayette, IN, USA.

Fast-charging sodium metal anodes: challenges, degradation mechanisms, and interphase engineering strategies

As renewable energy integration increases, efficient grid-scale storage becomes essential, motivating fast-charging sodium metal batteries for stationary applications. High-rate operation triggers degradation distinct from conventional cycling, including accelerated SEI rupture/reformation, diffusion-limited Na^+ depletion, dendritic growth, and void-driven dead sodium accumulation. This review analyzes these rate-specific failure modes and establishes design principles for artificial SEIs, emphasizing ultrathin, robust layers that homogenize ion flux. By surveying recent inorganic, organic, and hybrid interphases, the work outlines pathways toward safe, durable sodium metal anodes for large-scale deployment.

Image reproduced by permission of Sunghwan Lee, Yuxuan Zhang and Yeongjun Oh from *RSC Appl. Interfaces*, 2025, **3**, 214. The cover artwork was generated and refined using Google Gemini.

As featured in:

See Sunghwan Lee *et al.*, *RSC Appl. Interfaces*, 2026, **3**, 214.

ROYAL SOCIETY OF CHEMISTRY

rsc.li/RSCApplInter

Registered charity number: 207890

RSC Applied Interfaces

ROYAL SOCIETY OF CHEMISTRY

REVIEW

View Article Online
View Journal | View Issue

Cite this: *RSC Appl. Interfaces*, 2026, 3, 214

Fast-charging sodium metal anodes: challenges, degradation mechanisms, and interphase engineering strategies

Yeongjun Oh, Yuxuan Zhang, Jinwook Baek, Minyoung Kim and Sunghwan Lee *

With the increasing penetration of wind and solar power, large-scale and cost-effective energy storage has become essential, making sodium metal batteries more suitable than lithium counterparts for stationary applications. The strong demand for high peak power from intermittent renewable generation necessitates fast-charging/discharging capability of sodium metal batteries. Challenges such as unstable solid electrolyte interphases (SEIs), dendritic growth, gas evolution, and interfacial fracture are magnified under fast-charging and fast-discharging conditions. Unlike conventional cycling, transient high-rate operation induces unique rate-dependent degradation, including accelerated SEI rupture/reformation, current constriction at interfacial hot spots, diffusion-limited Na^+ depletion, and void-driven dead sodium accumulation. Even though these mechanisms demand interphase engineering strategies distinct from those optimized for moderate cycling, fast-charging degradation has often been regarded merely as an extension of conventional cycling without being addressed independently. In this review, we first delineate the fundamental failure modes of sodium metal anodes under high-rate operation, contrasting them with conventional cycling instabilities. Based on these insights, we establish design principles for artificial SEIs (aSEIs), emphasizing ultrathin yet robust layers with low desolvation barriers, high Na^+ conductivity, and homogeneous ion-flux regulation. We then survey recent advances in *ex situ* artificial interphases, which includes inorganic coatings, organic films, and hybrid organic–inorganic architectures, highlighting their ability to reconcile conflicting requirements of ionic transport, electronic insulation, and mechanical toughness. Finally, we present an outlook on future directions, including scalable interphase fabrication, operando interfacial characterization, data-driven discovery, and multifunctional self-adaptive coatings. By systematically integrating mechanistic understanding with emerging interphase strategies, this review underscores that rational SEI design is pivotal for enabling safe, efficient, and durable sodium metal anodes under fast-charging/discharging conditions, ultimately accelerating their deployment in large-scale renewable energy storage systems.

Received 9th October 2025,
Accepted 7th January 2026

DOI: 10.1039/d5lf00305a

rsc.li/RSCApplInter

1. Introduction

With the accelerating integration of renewable energy sources such as wind and solar, the demand for cost-effective and sustainable energy storage systems has become increasingly urgent.[1,2] Lithium-ion batteries (LIBs), while dominant in today's market, face inherent limitations including resource scarcity, escalating cost, and safety risks associated with dendrite growth under high-rate operation.[3–5] These challenges have spurred intensive research into sodium batteries, which leverage the natural abundance, low cost, and global distribution of sodium resources.[1–3,6] In particular, sodium-ion batteries employing hard carbon anodes have progressed from pilot demonstrations to early commercial deployment in grid-connected battery energy storage systems, indicating that many stationary applications can already be served by intercalation-type sodium chemistries with moderate energy density, long cycle life, and robust safety. Beyond resource availability, sodium-based systems fit stationary storage well: relaxed volumetric and weight constraints allow safety-first designs (for example, nonflammable or low-volatility electrolytes),[7,8] and, with appropriate interphase and electrolyte engineering, high-rate power handling needed for grid services can be achieved.[6,9]

Among various anode candidates, sodium metal stands out due to its high theoretical capacity (1166 mAh g^{-1}) and low redox potential of −2.71 V *vs.* standard hydrogen electrode (SHE), which can significantly elevate the energy density of sodium batteries compared with intercalation-type anodes such as hard carbon or alloys.[10,11] However, the practical deployment of sodium metal anodes has been hindered by critical issues:

School of Engineering Technology, Purdue University, West Lafayette, IN 47907, USA. E-mail: sunghlee@purdue.edu

unstable solid electrolyte interphase (SEI), dendritic deposition, continuous parasitic reactions, and severe volume fluctuations.[12,13] These degradation mechanisms cause poor coulombic efficiency (CE), capacity fading, and substantial safety risks, thus requiring extensive efforts to optimize electrolytes, design host structures, develop alloying strategies, and engineer stable interphases. For grid-scale installations, such limited cycling stability directly penalizes the levelized cost of storage, thereby constraining the operating space in which sodium metal anodes can be competitive with sodium-ion systems.

Among these approaches, interphase construction, particularly artificial SEI (aSEI) design, has proven more versatile and effective than bulk alloying or host engineering, which remain constrained in areal capacity at grid-relevant loadings and in high-rate capability due to phase-transformation hysteresis, mechanical pulverization, ion transport tortuosity, and scalability challenges.[14–17] A properly designed interphase can simultaneously provide selective Na^+ transport, electronic insulation, chemical stability, and mechanical robustness, thereby directly addressing the interfacial origins of degradation.

Unlike LIBs that are primarily deployed in portable electronics or electric vehicles, sodium batteries are envisioned primarily for large-scale grid storage, where utility-scale systems are typically sized for discharge durations on the order of one to several hours at rated power, corresponding to operating rates near the 1C regime rather than continuous ultra-fast charging. Beyond materials fundamentals, the application context of stationary storage imposes distinctive interfacial stressors on Na metal anodes. Intermittent wind and solar generation produce frequent power ramps and short-duration pulses, translating into sustained high current densities and large areal throughput, which intensify concentration polarization, promote localized current hot spots, and accelerate SEI cracking and dendritic propagation.[6,9,18,19] For quantitative discussion, the plating or stripping current density j in mA cm^{-2} can be related to the cell C-rate r through the cathode areal capacity Q_A in mAh cm^{-2}, such that $j = r\,Q_A$. For example, a cathode with a loading of 10 mg cm^{-2} and a specific capacity of 150 mAh g^{-1} has an areal capacity of 1.5 mAh cm^{-2} and therefore experiences 1.5 mA cm^{-2} at 1C, which is representative of standard operation in many battery energy storage systems. In sodium metal cells, available experimental and modeling studies indicate that rate-dependent instabilities become increasingly pronounced once j reaches values on the order of a few mA cm^{-2}, so in grid-oriented sodium batteries fast charging is most appropriately associated with the short high-flux transients imposed by such services rather than with the baseline 1C cycling used for bulk energy shifting. Consequently, interphase design for fast charging must explicitly target mechanical robustness and homogeneous ion-flux regulation under high-rate transients, rather than relying on criteria defined for moderate charging regimes.[19]

Despite rapid progress in sodium metal anode research, dedicated syntheses that focus explicitly on failure mechanisms under fast-charging/discharging of Na metal anodes remain limited and scattered across subtopics, leaving interphase design principles underdeveloped for realistic grid-scale operation.[14,18,20]

Herein, we provide a comprehensive review that seeks to fill this critical gap. First, we delineate the unique failure mechanisms of sodium metal anodes under fast charging and discharging conditions, including accelerated SEI rupture and reconstruction, intensified concentration polarization, localized current hot spots, and excessive dendritic propagation as well as systematically contrast these rate-dependent instabilities with those observed under moderate cycling, where failure is typically governed by gradual SEI evolution and moderate dead-sodium accumulation. Second, based on these insights, we establish a set of interphase design principles tailored for fast charging, emphasizing the need for ultrathin yet mechanically robust layers with high Na^+ conductivity, low desolvation energy barriers, and homogeneous interfacial ion flux regulation, which collectively differ from the conventional benchmarks defined for moderate cycling.[19,21–23] Third, we comprehensively survey recent artificial SEI construction strategies and material systems, including inorganic coatings, organic/inorganic hybrids, polymeric interphases, and emerging high-entropy or multifunctional designs, highlighting how these approaches address the kinetic and mechanical demands of fast charging.[12,14,20] Finally, we present a forward-looking outlook, identifying persisting challenges such as scalability of interphase fabrication, compatibility with diverse electrolyte chemistries, and the need for advanced operando characterization and modeling. We also propose future opportunities, including data-driven interphase discovery, multifunctional self-adaptive coatings, and cross-fertilization with strategies from other metal anodes, to ultimately enable safe, high-rate, and durable sodium metal batteries for grid-scale renewable energy integration.

2. Failure mechanisms under fast charging and discharging

Unlike general cycling degradation, fast charging/discharging imposes unique stresses on sodium metal anodes. Under moderate current densities (<2 mA cm^{-2}), degradation is typically dominated by gradual electrolyte consumption, SEI thickening, and partial loss of active Na (also known as "dead Na").[24,25] However, once the current density rises into the fast-charging/discharging regime (>2 mA cm^{-2}), multiple degradation pathways, such as SEI dissolution/reformation, SEI-limited current hot spots, and diffusion-limited electrolyte depletion, are kinetically accelerated and strongly coupled.[26–30] Fast charging/discharging thus introduces rate-dependent phenomena, such as insufficient Na^+ desolvation, severe transport bottlenecks by SEI, and diffusion-limited instabilities, which do not dominate under moderate charging/discharging conditions (*i.e.*, 2 mA cm^{-2}).[28,31,32] Moreover, the fast charging/discharging failure mechanism of sodium metal differs fundamentally from that of Li metal.

Lithium anodes can tolerate current densities on the order of ~20 mA cm^{-2} before severe dendritic instability dominates, whereas sodium typically exhibits similar instabilities at only ~2 mA cm^{-2}.[33,34] Consequently, defining and mitigating rate-induced degradation is even more crucial for sodium metal batteries, as their practical power density ceiling is intrinsically lower than that of Li systems. Recognizing this distinction between moderate and fast-cycling conditions is therefore essential to accurately define the fast-charging/discharging limit of sodium metal batteries. A dedicated analysis of these failure modes further enables identification of the primary rate-limiting processes constraining Na metal anodes and guides the rational design of electrolytes, interphases, and electrode architectures capable of safely supporting high-rate operation.[35]

2.1. Unfavorable Na solid electrolytes interphase

The SEI that forms spontaneously on sodium metal by electrolyte reduction is the proximate origin of interfacial instability (Fig. 1a).[24,25] In sodium based cells, this reduction can be viewed as interfacial electron transfer from Na metal into low lying acceptor states of solvated electrolyte species at the surface, and recent sodium electrolyte studies describe the onset of this process in molecular orbital terms by associating electrolyte reduction with effective LUMO levels of interfacial complexes that fall below the anode Fermi level The SEI that results contains inorganic phases and organic decomposition products whose relative fractions and depth distribution are governed by which solvent, anion or additive is reduced first. The local solvation structure and salt concentration determine which component provides the lowest effective acceptor level, and therefore bias the earliest SEI building blocks toward specific inorganic motifs such as NaF and Na_2CO_3 and organic motifs such as sodium alkyl carbonates.[36–38] Because these inorganic and organic products originate from electrolyte decomposition, the identity of the solvent and salt strongly influences the initial SEI structure, thickness, and stability, and thereby the way the native interphase evolves or destabilizes under high-rate operation. Ideally, the SEI should be selectively permeable to Na^+ while electronically insulating the electrode, thereby suppressing further electrolyte decomposition.[25,39] However, in practice, the SEI exhibits a structurally heterogeneous mosaic composed of inorganic phases (predominantly NaF, Na_2CO_3, and Na_2O) intermixed with organic decomposition products, resulting in pronounced spatial variability in composition and thickness.[24,40–42] Under the fast charging conditions considered here, larger overpotentials and higher Na^+ flux accelerate these initial reduction pathways and magnify small lateral differences in solvation and reaction kinetics, so this native Na SEI rapidly evolves into a chemically and structurally heterogeneous mosaic that seeds the rate dependent instabilities discussed below.[26]

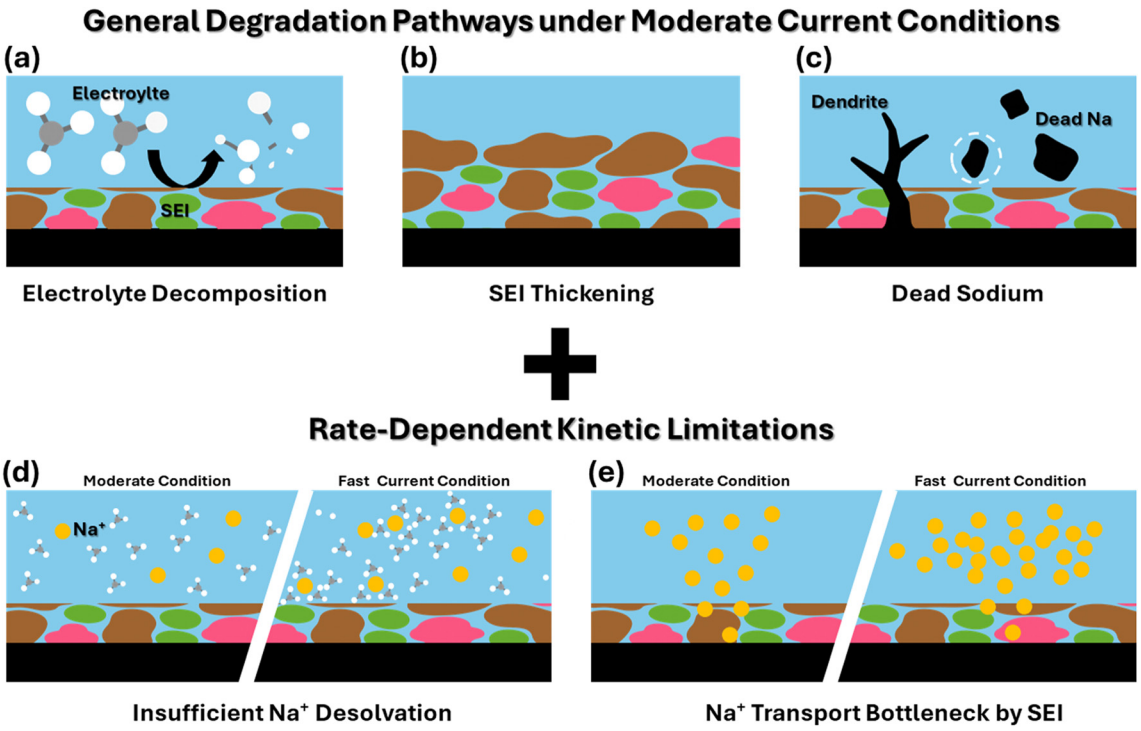

Fig. 1 Schematic illustration of SEI evolution and rate-induced instabilities during fast current condition. (a) Electrolyte reduction forms a heterogeneous SEI. (b) Spatial variations in composition and thickness lead to nonuniform ion transport. (c) Dendrite formation and electrically isolated deposits (dead Na) arise under high current densities. (d and e) Rate-dependent kinetic limitations: (d) Na^+ desolvation and (e) SEI-imposed Na^+ transport. The panels illustrate the transition from a non-limiting state under "moderate condition" (left) to a bottleneck state under "fast current condition" (right), highlighting how kinetic limitations are triggered specifically by high ion flux.

This chemical and structural heterogeneity triggers two primary instability mechanisms and becomes especially rate-sensitive under fast charging/discharging.

First, the evolution of SEI on sodium metal results from a dynamic competition between the formation and dissolution of SEI. The dissolution of SEI is due to the instability of organic-rich domains of RCH_2ONa, $ROCO_2Na$. Relative to inorganic species, organic reduction products are more soluble in ether- and carbonate-based electrolytes compared to inorganic-rich domains. The gross areal mass change of the SEI can be described by eqn (1).

$$\frac{dm_{SEI}}{dt} = -\sum_{k\varepsilon S} W_k\left(\dot{s}_k^{prec} - \dot{s}_k^{diss}\right) \quad (1)$$

where m_{SEI} is the SEI mass per unit area, k indexes each constituent phase (*e.g.*, NaF, Na_2CO_3, organic salts), W_k is the molar mass of phase k, and s_k^{prec}, s_k^{diss} are the interfacial precipitation and dissolution rates per unit area, respectively.[43,44] Under conventional cycling, the balance between dissolution and formation evolves gradually, yielding a thick yet moderately protective and resistive SEI (Fig. 1b). By contrast, during fast charging/discharging, the accelerated flux of solvated Na^+ and intensified local overpotential drive repeated dissolution–reprecipitation at short time scales on the order of seconds under high-rate steps. Rather than acting as a stable passivation film, the SEI undergoes continual changes in thickness and composition, causing transient thinning and local exposure of fresh sodium metal, which compromises its protective function and perpetually seeds unpredictable defects such as microcracks, interfacial pores/voids, and local delamination across the surface.[44–46] These defects seed dendrites and electrically isolated deposits (dead Na) at high current densities (Fig. 1c).

Second, a transport bottleneck is set by inorganic-rich SEI domains. Inorganic SEI constituents such as NaF, Na_2CO_3, and Na_2O exhibit inherently low Na^+ ionic conductivity. When these inorganic species form continuous or percolating pathways within the SEI, they substantially restrict Na^+ transport and significantly increase the overall ionic resistance. Under fast-charging conditions, this transport limitation becomes critical, and insufficient Na^+ desolvation at the SEI/electrolyte interface further elevates the interfacial overpotential (Fig. 1d). From a simplified one-dimensional analysis, the Na^+ flux through the SEI can be approximated as eqn (2).

$$J_{Na} \approx \left(\frac{\kappa_{SEI}}{zF}\right)\left(\frac{\Delta\phi_{SEI}}{\delta_{SEI}}\right) \quad (2)$$

Given the relationship $i = zF\,J_{Na}$ (with $z = 1$ for Na), an Ohmic approximation for current density (i) across the SEI yields eqn (3).

$$i = \frac{\kappa_{SEI}\Delta\phi_{SEI}}{\delta_{SEI}} \quad (3)$$

Here, κ_{SEI}, δ_{SEI}, and $\Delta\phi_{SEI}$ denote the SEI ionic conductivity, thickness, and difference in electrostatic potential across the SEI, respectively, and F is Faraday's constant. Thus, to sustain the high ion flux required at elevated current densities, an increased overpotential across the SEI inevitably arises within low-conductivity inorganic-rich domains, manifesting as an SEI-imposed Na^+ transport bottleneck (Fig. 1e).

Spatial inhomogeneity in SEI thickness (δ_{SEI}) and conductivity (κ_{SEI}) generates local variations in SEI resistivity ($\rho_{SEI} = \delta_{SEI}/\kappa_{SEI}$). Consequently, even under uniform overall potential drop conditions, current preferentially funnels into thinner or defect-rich pathways characterized by lower resistivity. At high current densities, this phenomenon of current constriction amplifies dramatically due to nonlinear electrode kinetics and concentration polarization. Specifically, as $\Delta\phi_{SEI}$ increases with current density, nonlinear reaction kinetics and electrolyte depletion near interfaces further magnify local potential gradients and ionic concentration variations. Ultimately, this combination of large internal potential drop and spatial resistivity variations drives highly anisotropic and nonuniform Na deposition that amplifies preexisting morphological and compositional nonuniformities.[25,27,46]

Finally, from a mechanics perspective, the native SEI is intrinsically fragile. During repeated plating and stripping, it experiences alternating tensile, shear, and compressive loads and is prone to cracking and delamination, which follows the general creep kinetics described by eqn (4).[47–49]

$$\dot{\varepsilon} = A\sigma^n \exp\left(-\frac{Q}{RT}\right) \quad (4)$$

where $\dot{\varepsilon}$ is the creep strain rate, σ is the applied stress, and A, n, Q are material constants, R is the gas constant, and T is the absolute temperature. Sodium at room temperature operates at a high homologous temperature ($T/T_m = \sim 0.8$), which facilitates creep and viscoplastic flow in the metal and deformation mismatch between the SEI and the underlying Na, thus accumulates readily, which breaks interfacial continuity and exposes fresh metal. Electrolyte reduction then restarts on short time scales, which drives SEI reformation and impedance rise. Crack tips and delaminated boundaries act as hotspots of current and field concentration, which further increases overpotential and establishes favorable conditions for subsequent dendrite growth. Sodium is very soft and ductile at room temperature; tensile tests show extreme necking at failure, a low elastic modulus ($\sim 3.9 \pm 0.5$ GPa), and a low yield strength (~ 0.19–0.28 MPa).[47] This mismatch magnifies stress concentration at brittle, inorganic-rich SEI domains, so thin oxide/fluoride patches crack or debond as the metal creeps. However, direct verification of these interfacial failures has long been elusive because standard electron microscopy introduces beam-induced artifacts that obscure the native SEI state. To address this, advanced characterization techniques utilizing cryogenic protection and operando monitoring have been established to bridge the gap between electrochemical metrics and physical mechanisms (Fig. 2). First, cryogenic transmission electron microscopy (Cryo-TEM) successfully preserves the fragile interphase, revealing a heterogeneous mosaic architecture where crystalline inorganic domains (*e.g.*, Na_2CO_3, Na_3PO_4) are randomly distributed within an amorphous matrix (Fig. 2a).[38] This structural insight provides the missing link

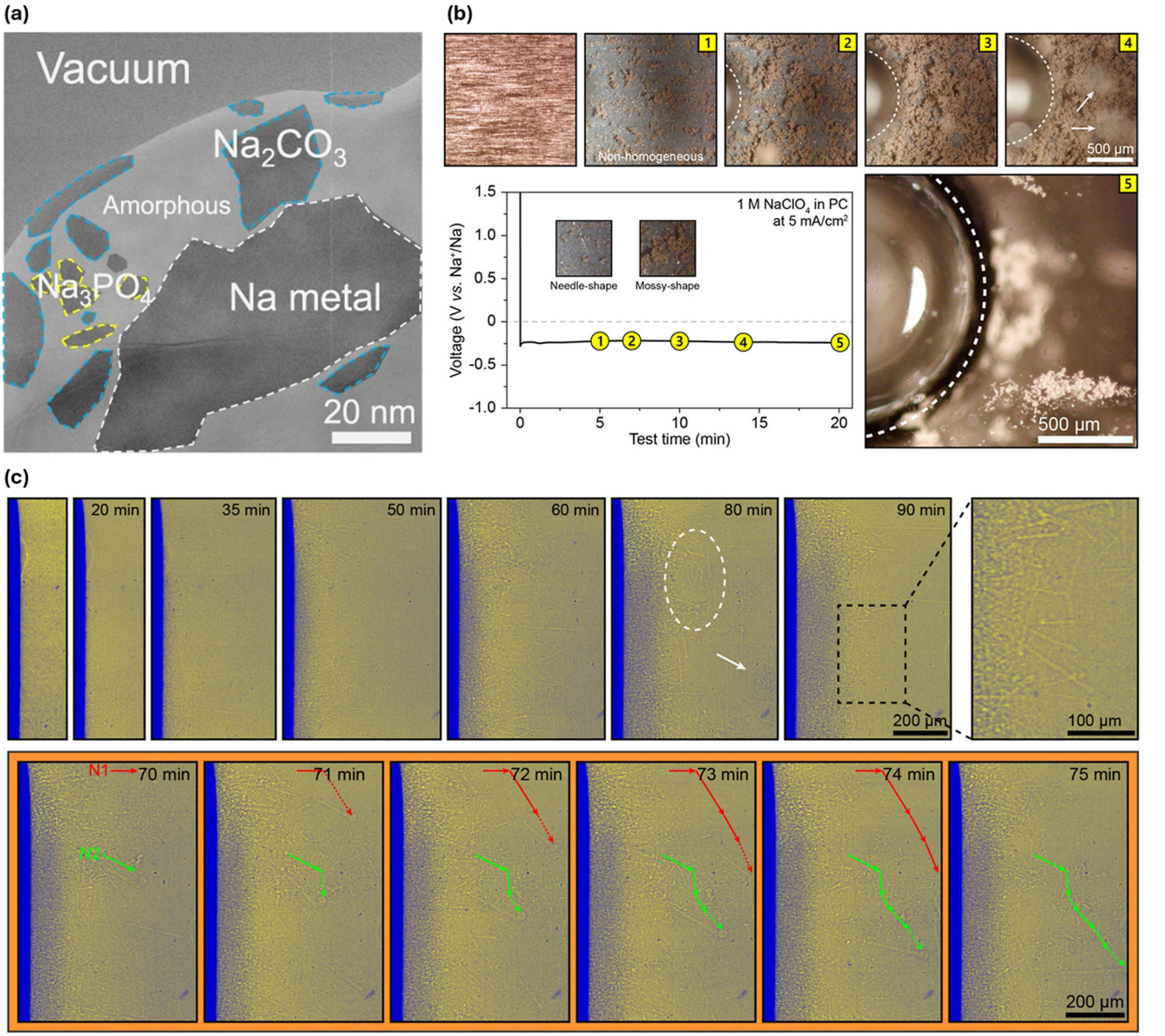

Fig. 2 (a) High-resolution Cryo-TEM (HRTEM) image showing the distribution of the native SEI components, where randomly distributed Na_2CO_3, Na_3PO_4, and amorphous phases form a typical mosaic-type SEI. (b) Operando optical microscopy images of sodium plated on a Cu current collector in 1 M $NaClO_4$ in PC electrolyte at a current density of 5 mA cm^{-2} for 20 min; the white circle and arrows indicate bubble generation and blurry dendrites, respectively. (c) Operando X-ray imaging of Na plating on a Cu current collector at a current density of 5 mA cm^{-2} in 1 M $NaClO_4$ in PC, where the white arrow indicates falling detached sodium dendrites, and N1 and N2 in the orange box present two distinct sodium dendrites being detached.

explaining why localized mechanical failure occurs so readily under stress. Therefore, under fast-rate transients, the SEI must resist both creep-driven opening and shear at crack tips, not merely provide ionic and electronic selectivity. These observations motivate later sections where hybrid interphases add ductility without sacrificing passivation.

2.2. Non-uniform plating/stripping and their associated instabilities

Dendrite growth is the most visible and hazardous failure mode of sodium metal anodes, and its onset is strongly accelerated under fast charging and discharging.[24,25] Unlike gradual surface roughening seen under low to moderate current densities, high-rate operation imposes extreme local fluxes that drive anisotropic plating. As captured by operando optical microscopy (Fig. 2b), localized current hotspots drive the rapid propagation of dendrites, accompanied by gas bubble evolution that further destabilizes the interface.[42]

Dendrite formation constitutes a critical impediment to the safe and reliable operation of sodium metal batteries, especially under fast charging and discharging conditions. Typically, dendrite formation is described as a sequential growth mechanism illustrated schematically in Fig. 1a–c, and

Fig. 1d and e further schematize the rate amplified desolvation limitation and SEI imposed Na^+ transport bottlenecks that accompany this process under fast charging. Morphological instabilities fundamentally arise from local electrochemical heterogeneities associated with an unevenly formed and dynamically evolving SEI.[24,25,40] Spatial variations in SEI composition and thickness produce local patches with differing reactivity, which directly translate into spatial inhomogeneity in the local exchange current density (i_0).[24,25,40] Since the kinetics of the charge-transfer reaction depend explicitly on i_0, regions exhibiting higher i_0, which are typically characterized by thinner SEI, greater ionic conductivity, or structural defects, can initiate Na^+ reduction reactions more readily at lower activation overpotentials. Under fast charging, the effects of such localized disparities become greatly amplified due to the high imposed current density (j) (Fig. 3a and b).[50–52]

In the high-current-density (Tafel) regime, the local activation overpotential (η) can be approximated by eqn (5).

$$\eta = \frac{RT}{\alpha z F} \ln\left(\frac{j}{i_0}\right) \quad (5)$$

where R is the gas constant, T is the absolute temperature, α is the charge-transfer coefficient, z is the valence number of the ion, F is Faraday's constant, j is the applied current density, and i_0 is the local exchange current density.[53] According to this relationship, even at a uniform applied current density j, patches with lower i_0 require significantly larger activation overpotentials, thus suppressing local reactions. Consequently, ion flux and current are redistributed to the paths of least resistance, concentrating on adjacent patches with the highest i_0. At these "hot spots," the local current density far exceeds the average value, leading to an explosive nucleation and growth of Na^+ and the formation of initial protrusions.

Local dendrite growth is further accelerated by diffusion limitations in the electrolyte. Under constant-current deposition, Na^+ is continuously consumed at the metal surface while diffusion from the bulk attempts to replenish it, and when the flux of Na^+ ions near the interface cannot match their deposition rate, a concentration-depletion layer forms (Fig. 3c). In this classical picture, Sand's time (t_{Sand}) is defined as the moment when the Na^+ concentration at the electrode surface is first driven to zero under a fixed current, that is, when the interface enters a strongly diffusion-limited regime with steep concentration and potential gradients. The critical onset time of this depletion layer can be expressed as eqn (6).

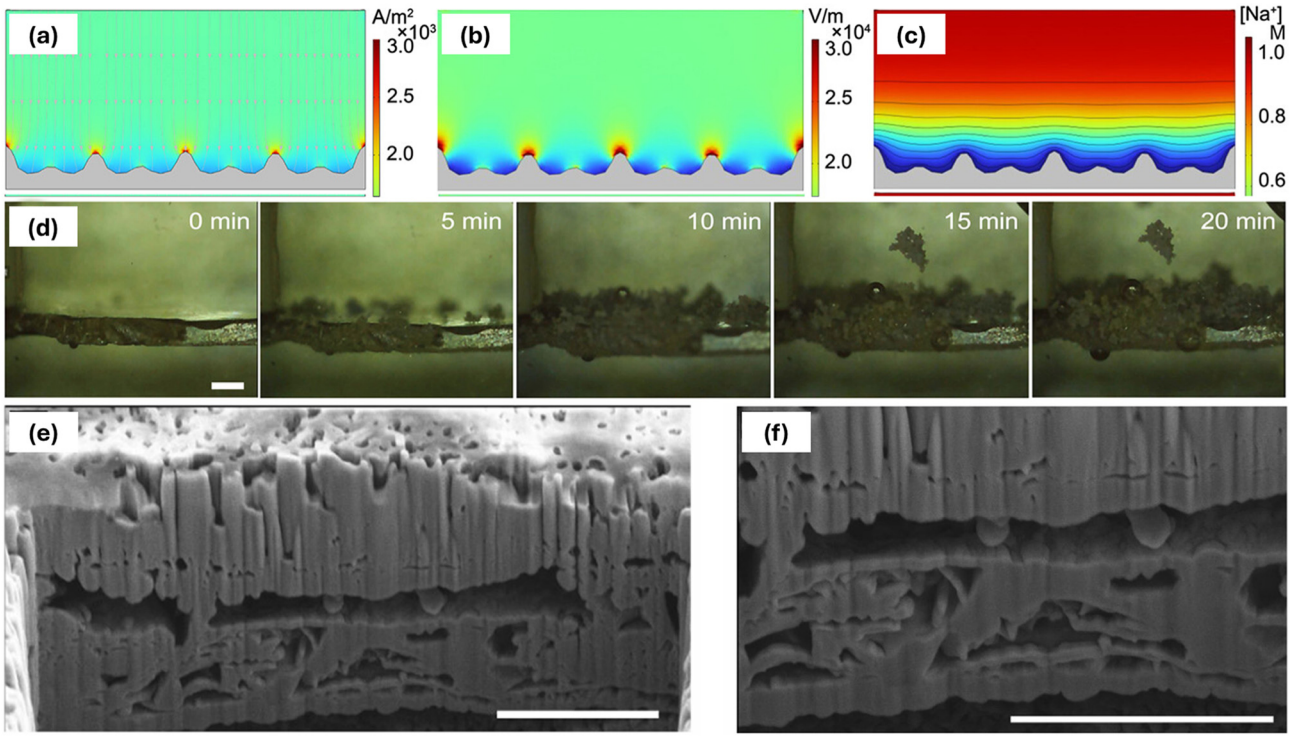

Fig. 3 Non-uniform Na plating/stripping under fast-rate operation. (a) Simulated local current density j at a corrugated Na/electrolyte interface, showing hot spots at crest tips. (b) Simulated electric-field intensity $|E|$ for the same geometry, illustrating field focusing at protrusions. (c) Simulated Na^+ profile highlighting formation of a diffusion-depletion layer above the interface. (d) Operando optical microscopy sequence (0–20 min) during Na plating showing edge-first nucleation, progressive roughening, and intermittent detachment of fragile protrusions. The scale bar is 500 μm. (e) Cross-sectional SEM after cycling, revealing a porous/voided layer beneath the interphase and vertically aligned channel-like defects. (f) Higher-magnification view of (e), resolving the fine porous/void network and crack-like vertical features beneath the interphase. The scale bar is 50 μm for both.

$$t_{\text{Sand}} = \frac{\pi D}{4}\left(\frac{zFC_0(1-t_+)}{j}\right)^2 \quad (6)$$

where D is the effective diffusion coefficient of the electrolyte salt, z is the ion valence (1 for Na^+), C_0 is the bulk salt concentration, t_+ is the cation transference number, and j is the applied current density. Crucially, this expression indicates a scaling relationship $t_{\text{Sand}} \propto j^{-2}$; even modest increases in current density drastically shorten the time for instability initiation.[28,51,54] After this depletion threshold has been reached, flat regions of the interface are effectively starved of ions, while any small protrusion that extends slightly into regions of higher concentration experiences a much larger local driving force. Once protrusions form, regions of high curvature at dendrite tips further concentrate electric fields, as directly captured by operando optical microscopy, creating conditions for self-amplified growth into needle-like or mossy dendritic morphologies (Fig. 3d).[50,52,54]

While stripping at low to moderate current densities may proceed relatively uniformly, at high current densities the Na extraction rate surpasses the ability of metal to redistribute laterally. This leads to extensive void nucleation beneath the SEI (Fig. 3e and f), generating electrically isolated deposits dead Na.[40,44,45] This catastrophic failure mode has been directly visualized *via* operando X-ray microscopy (Fig. 3c), which captures the detachment of sodium dendrites from the bulk electrode during cycling.[42] The void current density can be expressed as eqn (7).

$$J_{\text{void}} = \frac{j}{zF}\left(1 - \frac{\eta}{\eta_c}\right) \quad (7)$$

where η_c is the critical overpotential for uniform stripping.[55,56] At high j, J_{void} dominates, causing rapid dead Na accumulation, severe Coulombic inefficiency, and collapse of SEI integrity. This behavior is fundamentally different from general cycling, where stripping is gradual and void generation is limited. In the fast-discharge regime, stripping transitions from benign at moderate rates to catastrophic at high rates, making it a defining failure pathway distinct from conventional cycling.[57–59] The plating–stripping asymmetry establishes a self-reinforcing cycle: localized plating generates dendritic protrusions, high-rate stripping hollows voids beneath them, and SEI fragility accelerates crack growth. Crack tips and void edges concentrate both current and mechanical stress, creating hotspots for runaway dendrite propagation and eventual separator penetration.[40,45] Macroscopically, these processes manifest as voltage noise, a steep rise in overpotential, falling CE, internal shorting, and catastrophic failure.[45,59] The low shear modulus (~3.3 GPa) and high homologous temperature (T/Tm = ~0.8) of Na compared to Li exacerbate these instabilities, ensuring that dendrite formation and void-induced dead Na are the central bottlenecks of sodium metal anodes under fast charging and discharging.[47,49]

2.3. Gas generation

Gas evolution is commonly observed under fast-charging conditions and simultaneously perturbs interfacial electrochemistry, ionic transport, and mechanical integrity, thereby completing a coupled degradation network.[60–63] The gaseous species, predominantly CO_2, CO, H_2, and C_2H_4, arise from reductive decomposition of electrolyte solvents and salts as well as ongoing chemical reactions involving the SEI.[60,63,64] During fast charging, elevated interfacial overpotentials and localized Joule heating lower the onset potentials and significantly accelerate parasitic reactions, which include solvent reduction that generates gaseous species like CO_2, CO, H_2, and C_2H_4, and salt-derived pathways that form acidic byproducts such as HF and POF_3.[50,53–56] For instance, an *in situ* sequence of Na plating and stripping in a $NaPF_6$/ethylene carbonate (EC) : dimethyl carbonate (DMC) electrolyte clearly shows gas bubbles appearing during the stripping process (Fig. 4a).[65] Representative frames further illustrate this phenomenon, showing the growth of these bubbles directly at the Na|SEI|electrolyte interface (Fig. 4b). Mechanically, bubble/SEI interfaces concentrate shear and tensile stresses because curvature-induced Laplace pressure and adhesion/modulus mismatch between the SEI and Na focus tractions at the bubble rim and nearby crack tips, leading to localized cracking and delamination.[66] The resulting loss of SEI continuity exposes fresh sodium surfaces, immediately triggering renewed electrolyte reduction and further gas evolution.[60,67]

In addition to anode-local chemistry, fast charging and discharging create a second gas pathway that originates from chemical crosstalk between the cathode and anode of the full cell (Fig. 4c). Steep potential and concentration gradients increase the net transport of chemical species generated or released at the positive electrode, including acidic byproducts such as HF and POF_3 from salt and solvent reactions, structural or residual water H_2O released from the cathode, and dissolved transition-metal cations released from the cathode under oxidizing or acidic conditions, such as Mn^{2+}, Co^{2+}, and Ni^{2+}. Their flux toward the anode rises with rate as the driving fields strengthen.[68–71] When these species arrive at the sodium anode, they open new gas-forming routes that operate independently of the local SEI reaction sequence. Acidic species attack carbonate-containing or mixed inorganic SEI domains and generate CO_2 and H_2 while dissolving inorganic phases that normally provide electronic blocking. Water that reaches the anode drives hydrogen evolution and lowers local wettability. Transition-metal ions deposit at the interface, disrupt the interphase structure, and catalyze further electrolyte reduction, so gas formation increases even when the pre-existing SEI is momentarily continuous.[68,71] This chemical crosstalk can also be bidirectional, where gaseous species like C_2H_4 generated at the anode migrate to and parasitically react with the cathode surface.

Gas generation under fast charging therefore arises through both anode-local SEI reactions and cathode-derived crosstalk pathways, and the bubbles formed have severe

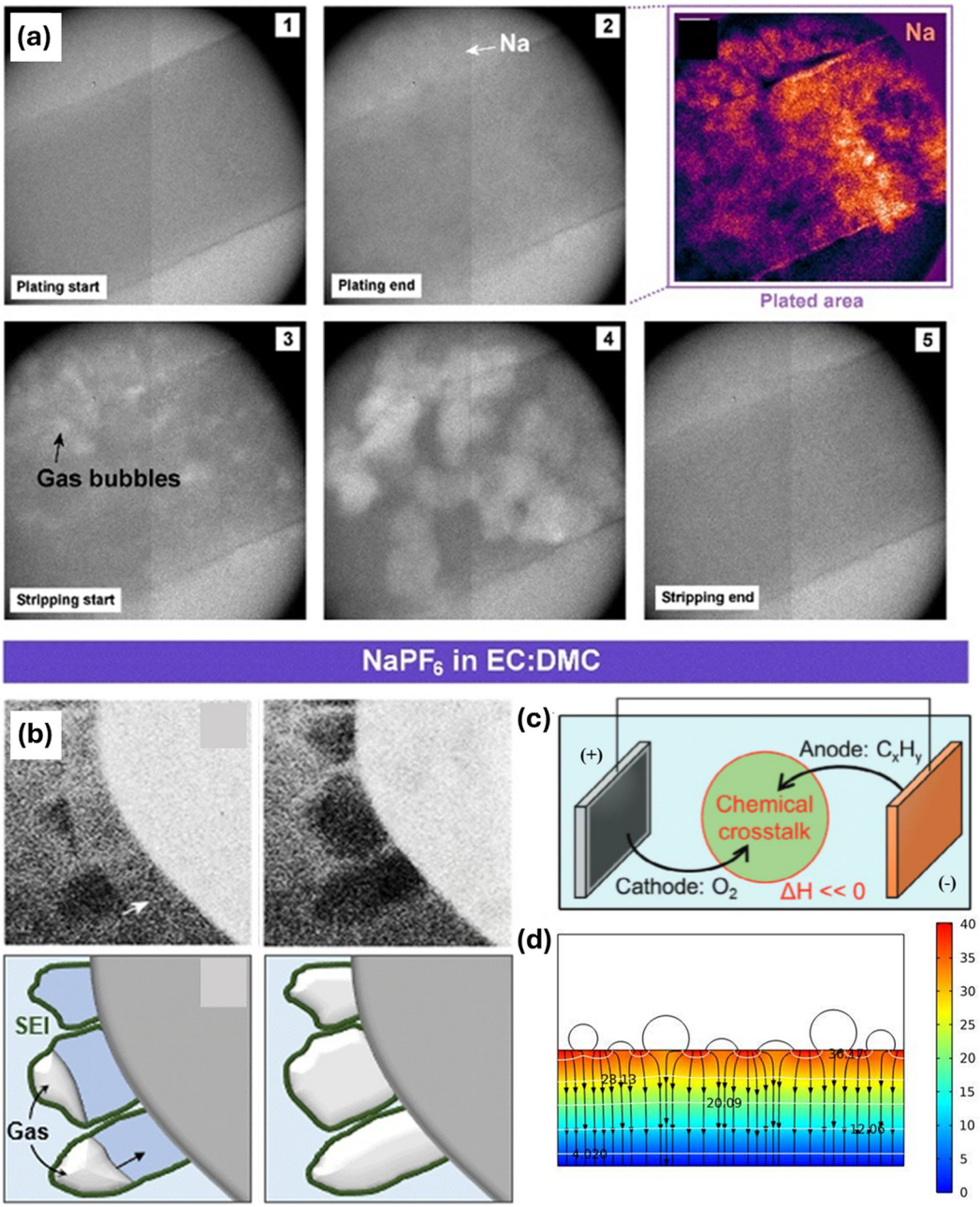

Fig. 4 Bubble-mediated instability and chemical crosstalk in sodium-metal cells. (a) *In situ* sequence of Na plating and stripping in $NaPF_6$/EC:DMC. Gas bubbles appear during stripping. (b) Representative frames with accompanying cartoons showing bubble growth at the Na|SEI| electrolyte interface. The bubbles delaminate the SEI and drive uneven deposition during cycling. (c) Configuration of the crosstalk effect between the C_2H_4 gas generated from SEI decomposition and cathode. (d) The simulation of the distribution of electric field with bubbles attached to the copper surface, where the numerical color scale (0–40) is dimensionless and represents the relative electric field intensity. The bubble-effects on the morphological evolution of deposited Na metal probed by phased field simulation.

electrochemical consequences. The regions they occupy become electrochemically inactive, forcing ionic current paths to constrict around them. Because the gas interior is nonconductive and dewets the interface, ionic field lines bypass the bubble and concentrate along the wetted rim, as confirmed by simulations of the electric field distribution on a bubble-attached surface (Fig. 4d). This flux redistribution couples with preexisting SEI heterogeneities and accelerates localized nucleation and dendrite growth.[67] New gas nuclei initially appear within interfacial pores and microcracks, further reducing the effective electrode–electrolyte contact area. Consequently, ionic currents become increasingly concentrated within thin or structurally defective segments of the SEI. This concentration of ionic flux intensifies local electric fields near these defective regions, promoting anisotropic metal plating. As a result, this transport-induced

mechanism further reinforces the positive-feedback loop involving gas formation, dewetting, current constriction, and SEI fracture, progressively shortening its characteristic timescale and thus lowering the threshold for dendritic instability.[66,67]

3. Interphase design principles

Na metal offers the highest theoretical capacity (1166 mAh g^{-1}) and the lowest redox potential (−2.71 V *vs.* SHE) among sodium-based anodes, making it an attractive choice for high-energy-density sodium batteries.[25,72] However, its direct contact with organic electrolytes results in uncontrolled interfacial reactions, dendrite growth, and gas evolution, leading to poor reversibility and severe safety risks.[10,25,60] In comparison, alloy anodes (Sn, Bi, *etc.*) offer better stability but suffer from low CE and limited capacity.[15,23,73] These trade-offs make interphase engineering indispensable, as only a well-designed interphase can simultaneously preserve the intrinsic high capacity of sodium metal while stabilizing the interface against degradation.[1–3,8]

At moderate current densities, the SEI must satisfy three classical requirements: high ionic conductivity, electronic insulation, and sufficient mechanical robustness.[25,39] First, fast Na^+ transport through the SEI is essential to minimize polarization during plating/stripping; inorganic species such as NaF, Na_2S, and Na_3P provide favorable pathways with low diffusion barriers.[10,13] Second, wide-bandgap inorganic salts (*e.g.*, NaF, Na_2O) effectively block electron leakage, thereby suppressing continuous electrolyte decomposition.[25,39] Third, mechanical integrity is needed to resist cracking and accommodate moderate volume fluctuations. A modulus above that of Na metal (~3.3 GPa) is often cited as a criterion for dendrite suppression, and inorganic-rich SEIs can meet this threshold.[13,22,23] Under such moderate conditions, these three functions, ionic conduction, electronic passivation, and mechanical stability, are generally sufficient to support reversible cycling.[25,39]

Under fast-charging or high-rate conditions, however, these baseline requirements become inadequate and must be elevated (Fig. 5). Kinetic bottlenecks shift toward desolvation at the anode surface and ion transport across the SEI, which represent the highest energy barriers in the charging process.[29,74] The SEI must therefore be ultrathin, highly uniform, and compositionally optimized to reduce both desolvation energy and Na^+ diffusion resistance.[29,74,75] At the same time, the extremely high current density produces severe ion-flux inhomogeneities. Even nanometer-scale variations in SEI thickness, composition, or wetting can magnify into macroscopic nonuniformities in current distribution. This causes current localization and preferential protrusion growth, accelerating dendritic nucleation.[25,45,74] Therefore, morphological control at the very first stages of plating, achieving numerous, evenly distributed Na nucleation sites and a homogeneous Na^+ flux field, is far more critical under fast charging than under moderate cycling.[29,74]

Mechanical integrity needs to be further enhanced to withstand fast plating and stripping. Rapid Na deposition generates steep local stress gradients and instantaneous volume expansion. SEIs that are sufficiently stiff at low current densities often fail catastrophically under fast operation, cracking or delaminating because they cannot redistribute stress quickly enough.[47,48,76] Similarly, fast stripping accentuates contact instability, where Na is removed nonuniformly, leaving behind isolated regions of dead Na that lose electronic connectivity. This effect is strongly correlated with Coulombic inefficiency at high rates.[57,77] Therefore, in addition to a high modulus, the SEI must exhibit strong cohesive toughness and elastic compliance to accommodate transient mechanical stress without losing interfacial integrity.[47,48,76]

Quantitatively, sodium's low stiffness and strength place a higher premium on interphase mechanics. Polycrystalline Na shows a Young's modulus of approximately 3.9 ± 0.5 GPa and a yield strength of roughly 0.19–0.28 MPa, and thin foils fail by extreme necking.[47,76] Thus, an aSEI must couple (i) electron blocking and fast Na^+ transport with (ii) crack-resistance and adhesion. In practice, very stiff but brittle

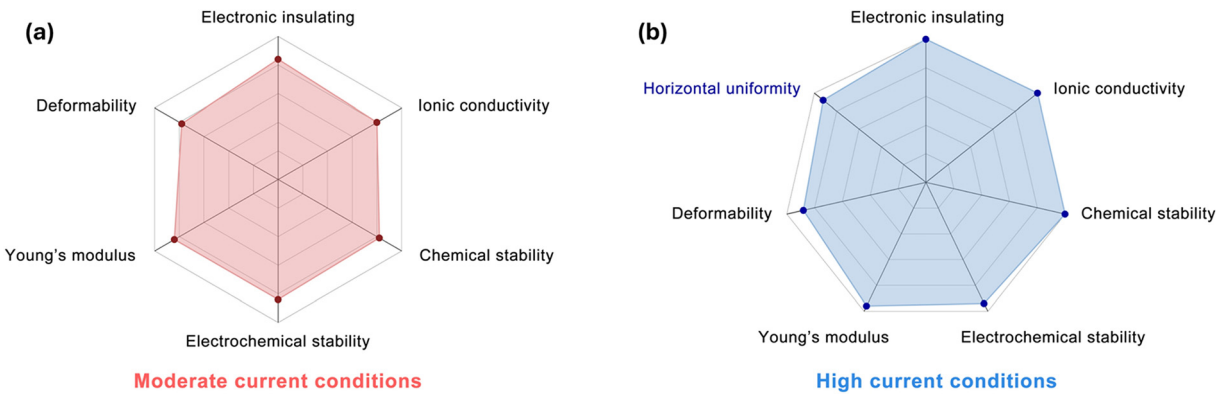

Fig. 5 Schematic comparison of interphase property requirements for sodium metal anodes under moderate (a) and high-rate (b) conditions, where the spider plots provide a qualitative illustration of changing design priorities rather than a quantitative scale. The key additional requirement under high-rate operation is horizontal uniformity, necessary to mitigate localized current hotspots and suppress dendritic propagation.

oxides need a compliant partner. Polycrystalline Na shows $E \approx 3.9 \pm 0.5$ GPa and $\sigma_y \approx 0.19$–0.28 MPa, and thin foils fail by extreme necking.[47,76] Thus, an aSEI must couple (i) electron blocking and fast Na^+ transport with (ii) crack-resistance and adhesion. In practice, very stiff but brittle oxides need a compliant partner. Molecular-layer-deposited alucone provides such ductility (crack-onset $\approx$ 9.9%, $E \approx 4.6 \pm 2.1$ GPa) while remaining conformal, which helps maintain contact at high rates.[78] For solid separators, the widely cited Monroe–Newman analysis highlights that sufficiently high shear modulus suppresses protrusion growth, emphasizing the need for mechanically reinforced interfaces.[7,9]

To meet these stringent demands, a horizontally homogeneous hybrid SEI is desirable. In this context, horizontally homogeneous denotes uniform composition and thickness across the electrode surface. Such structures combine stiff inorganic phases (*e.g.*, fluoride, oxides, phosphates) that block electrons and resist dendrite penetration with compliant polymeric domains that buffer strain and maintain intimate contact.[1–3] The hybrid is defined as a co-continuous interphase in which the inorganic electron-blocking network and the mechanically compliant polymer phase are uniformly distributed laterally and integrally interconnected across the surface.[1–3,20,23] The architecture should be ultrathin and laterally uniform to reduce desolvation and Na-ion diffusion barriers while avoiding ion-flux hotspots and current localization.[29,74] Hybrid SEIs can be realized *ex situ* using vapor- and solution-based routes including atomic layer deposition (ALD), initiated chemical vapor deposition, sol–gel synthesis, vapor-phase infiltration, and casting or blade-coating of composite precursors followed by post-treatments that equalize lateral thickness and composition.[1–3,29,79] By integrating electron blocking, high Na-ion transport, mechanical compliance, and chemical stability within a laterally homogeneous architecture, hybrid SEIs offer a promising pathway to reproducible, safe, and efficient sodium-metal cycling under fast-charging and fast-discharging conditions.[30,74]

4. State-of-the-art strategy of *ex situ* artificial interphase

Forming an aSEI on the sodium metal surface in an *ex situ* step prior to cell assembly is a key strategy for independently designing charge transfer, ionic conductivity, mechanical stability, adhesion, and chemical durability. It is presented as the most direct and reproducible solution to non-uniform plating, gas evolution, and the fragility of the native SEI. Artificial SEIs are classified by composition into inorganic, organic, and organic–inorganic hybrid types; inorganic layers suppress electron leakage and deformation owing to their wide bandgaps and high shear moduli,[1,2] whereas organic layers provide flexibility and viscoelasticity that mitigate cracking during repeated plating/stripping.[3] A hybrid (*i.e.*, organic + inorganic) SEI combines these advantages to simultaneously improve the critical current density (CCD) and cycle life.[3] The common design axes are the concurrent optimization of electron insulation, Na^+ transport, shear modulus, and interfacial adhesion, which together govern lifetime and safety under fast-charging conditions.

In quantitative terms, SEI design can be formulated with a simple metric by minimizing the voltage drop $\Delta\Phi_{SEI} = J_{Na} \cdot \delta_{SEI} / \kappa_{SEI}$ (where J_{Na} is the current density, δ_{SEI} the thickness, and κ_{SEI} the ionic conductivity).[6] The charge-transfer overpotential η is governed by the exchange current density i_0 and the surface desolvation barrier.[6] Mechanical stability is evaluated by whether the SEI shear modulus is sufficiently larger than that of metallic Na and whether adequate toughness and interfacial adhesion are secured to suppress crack propagation.[7] These relations immediately reveal competing requirements, for example electron insulation *versus* ionic transport, thickness δ_{SEI} *versus* polarization $\Delta\Phi_{SEI}$, and stiffness or toughness *versus* compliance or adhesion, which together motivate the structural solutions that follow. Moderate rate testing in the literature typically involves current densities at or below about 1 mA cm^{-2}, whereas conditions with current densities of 2 mA cm^{-2} and above in combination with areal capacities near 0.5 to 3 mAh cm^{-2} are regarded as fast charging for sodium metal cells.

The trade-offs among material properties lead to structural prescriptions. For example, dense inorganic films strengthen electron blocking and modulus but, if made too thick, raise $\Delta\Phi_{SEI}$ or constrain Na^+ transport, whereas compliant polymer films alleviate cracking but provide limited electronic insulation unless reinforced.[1–3] Electron insulation, Na^+ transport, shear modulus, toughness, and interfacial adhesion are difficult to realize simultaneously, and a single-layer of a single material rarely satisfies all requirements. For example, the halide class, including NaF, provides electron blocking and crack resistance owing to a very high shear modulus, but as a single layer, it can impose a high Na^+ diffusion barrier that limits rate performance. To resolve these limitations, multiphase designs that incorporate ion-friendly phases are required, and the following structural solutions are derived on first principles: (i) a bilayer comprising an inner alloy layer and an outer electron-insulating inorganic layer, in which the inner layer provides nucleation homogenization and stress compliance while the outer layer supplies electron blocking and chemical passivation;[8] (ii) a hierarchical composite that stacks or blends halides with chalcogenides or oxides to balance stiffness and ion transport;[1,9] (iii) a composite that disperses inorganic nanophases within a compliant organic matrix to achieve crack bridging while creating Na^+ conduction pathways.[3] With these combinations, low polarization and long cycle life can be achieved at current densities of 0.5–3 mA cm^{-2}.[1–3,8,9]

4.1. Inorganic artificial interphase for fast charging and discharging

Inorganic halides were among the first materials investigated for passivating sodium metal anodes, owing to their intrinsic

electrical insulation and high shear modulus.[10] Halide layers such as sodium fluoride (NaF), sodium chloride (NaCl), and sodium bromide (NaBr) possess wide bandgaps and high rigidity, enabling them to act as mechanical supports for deposited sodium while blocking electron conduction. However, halides that contain small anions, notably NaF, exhibit slow ionic transport because the surface diffusion barrier for Na^+ is high, ~0.25 eV (Fig. 6a).[10] Thick halide layers, therefore, raise overpotential during cycling. To mitigate this, halide interphases are preferably formed as ultrathin films of a few nanometers or combined in bilayers with an inner alloy or other ion conducting layer so that electron blocking and Na^+ transport are balanced and the current distribution remains uniform at high rates.

A composition-based approach lowers the barrier by moving from F^- to Cl^-, Br^-, and I^-, which density functional theory (DFT) predicts to reduce Na^+ migration energy (Fig. 6a–e).[10,11] In NaBr systems the energy difference between adjacent anions is small, facilitating interfacial Na^+ migration. *Ex situ* NaBr can be generated by reacting sodium with 1-bromopropane through a Wurtz type pathway, where two molecules of 1-bromopropane (R-Br) react with two sodium atoms (Na) to form an alkane (R–R) and sodium bromide (NaBr), following the equation: 2 R-Br + 2 Na → R–R + 2 NaBr. Cryo-focused ion beam (FIB)-scanning electron microscope (SEM) cross-sections and X-ray diffraction (XRD) directly confirm a dense, continuous NaBr layer (~2–12 μm) formed by the 1-bromopropane Wurtz pretreat on Na (Fig. 6f). The resulting NaBr derived interphase supports stable cycling above 250 h with high CE at current densities up to 0.25 mA cm^{-2} (ref. 10) (Fig. 6g). While this micrometer-scale thickness provides a dense physical barrier, from a practical perspective, an SEI layer exceeding several micrometers introduces significant ionic impedance and reduces the volumetric energy density of the cell. Future optimization should focus on reducing the layer thickness to the sub-micron scale, potentially by precisely controlling the precursor concentration and reaction time, to minimize the inactive mass while maintaining passivation. For NaI the interfacial migration barrier is ~0.02 eV. Pretreating sodium with 2-iodopropane yields an NaI rich interphase that lowers polarization and guides uniform high rate plating. Representative NaI protected Na||Na results include about 500 h at 0.25 mA cm^{-2} and 0.75 mAh cm^{-2} and about 850 h at 0.5 mA cm^{-2} and 1 mAh cm^{-2}, and Na–I_2 full cells that exceed two thousand cycles at 2 C with high capacity retention.[11] DFT shows the Na adatom diffusion barrier is ~0.25 eV on NaF and ~0.02 eV on NaI (Fig. 6b and c), and Na–I_2 full cells sustain >2200 cycles at 2 C with high retention (Fig. 6h). Because overpotential in practice is governed by the area-specific resistance set by thickness, ionic conductivity, and defect density, processing focuses on compact and uniform low resistance NaX films, where X is F, Cl, Br, or I.

A simple immersion method creates such compact halide layers. In this approach, freshly prepared sodium metal is contacted with a dimethyl carbonate solution containing SnF_2, and SnF_2 undergoes a conversion reaction to form a NaF-rich artificial SEI together with Na–Sn alloy at the surface, yielding a conformal fluorinated layer that isolates the metal from the liquid carbonate electrolyte, as schematically illustrated in Fig. 7a.[12] The dense fluoride rich film that maintains stable cycling for more than 700 h with low overpotential at 0.25 mA

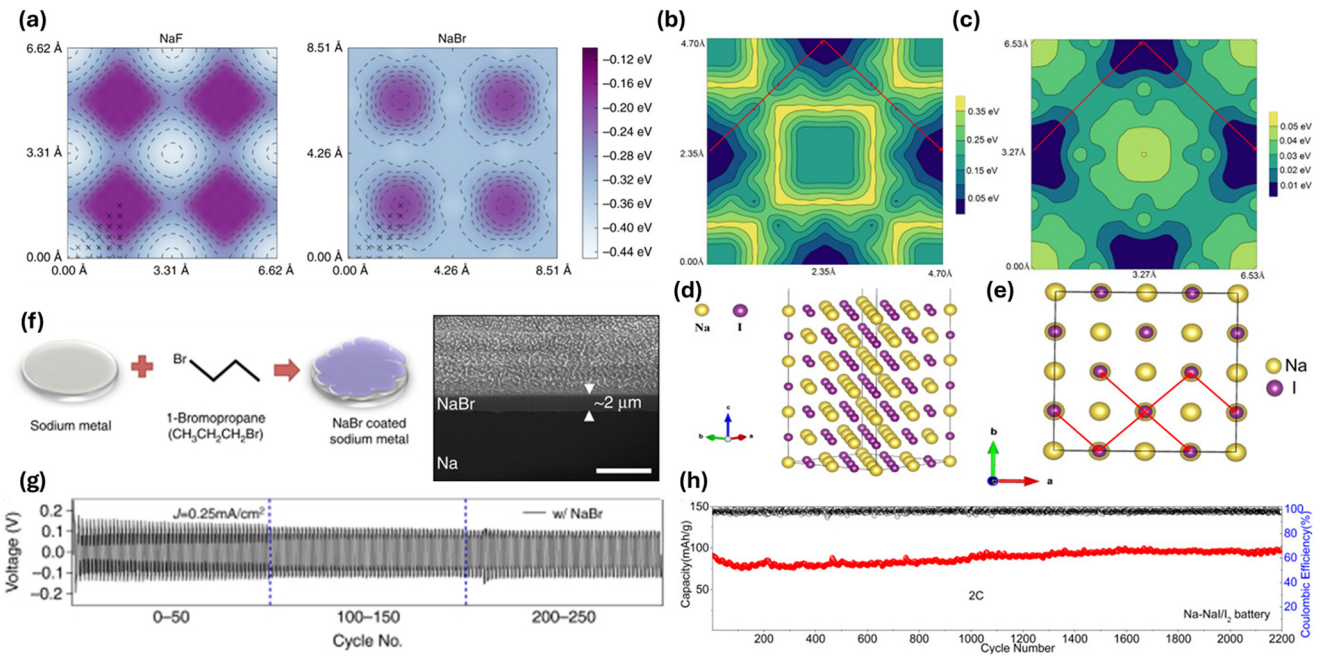

Fig. 6 Halide interphases for Na anodes. (a) DFT surface-binding energy maps for NaF and NaBr. (b–e) DFT surface-diffusion barriers for Na adatoms on NaF (b) and NaI (c). (d) NaI slab model. (e) Na adatom transport paths on NaI. (f) Schematic of 1-bromopropane (Wurtz) treatment and cross-sectional SEM showing ~2 μm NaBr coating. (g) Voltage–time trace of NaBr-coated Na||Na at 0.25 mA cm^{-2}. (h) Long-term cycling of Na–I_2 full cell at 2 C.

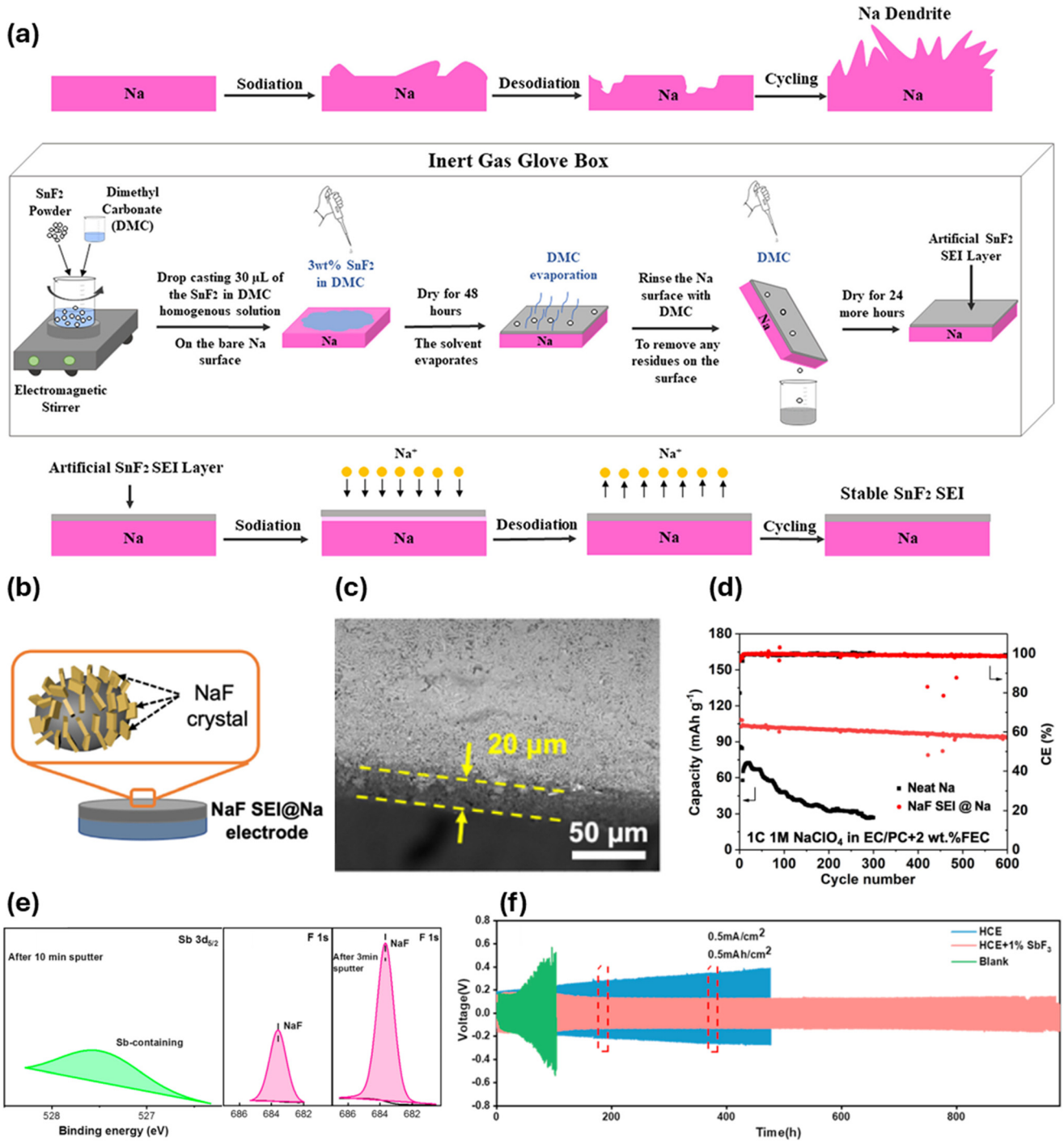

Fig. 7 (a) Schematic of NaF-rich SEI formation *via* SnF_2 immersion. (b–d) Formation and electrochemical performance of compact NaF/C–F interphase *via* molten Na–PTFE reaction: (b) schematic illustration, (c) cross-sectional SEM (~20 μm), and (d) long-term cycling in NVP full cells (1 C, carbonate electrolyte). (e) XPS depth profiles confirming inner Na–Sb alloy and outer NaF bilayer from SbF_3 additive in high-concentration electrolyte. (f) Stable Na||Na symmetric cell voltage profiles using SbF_3-derived bilayer at 0.5 mA cm^{-2}.

cm^{-2}. Powder lamination provides another route. Treating molten sodium near 290 °C with polytetrafluoroethylene (PTFE) micropowder drives an Na–F exchange that forms a continuous high-modulus NaF coating.[13] A schematic and cross-sectional SEM confirm a compact ~20 μm NaF/C–F layer formed on Na by the PTFE–Na reaction (Fig. 7b and c). When coupled with a sodium vanadium phosphate cathode, this NaF interphase retains 92% of the capacity after 400 cycles in an ether-based electrolyte and 94% after 600 cycles in a carbonate-based electrolyte. The cycling stability in the carbonate-based electrolyte is shown in Fig. 7d, consistent with homogenized Na^+ flux and reduced interfacial resistance. While effective in

symmetric cells, such a thick passivation layer (~20 μm) introduces substantial inactive weight and volume, which is detrimental to the practical energy density of full cells. To bridge the gap between laboratory demonstration and practical scale-up, processing methods must evolve from bulk surface reactions to more controllable techniques that can limit the fluoride layer thickness to the nanometer range while preserving its high modulus and density.

Halide interphases are also combined with other inorganic phases to reconcile Na^+ transport and mechanical rigidity under high rate conditions. One representative bilayer forms by drop casting a concentrated sodium bis(fluorosulfonyl) imide (NaFSI)– 1,2-dimethoxyethane (DME) solution containing SbF_3 onto sodium to generate an inner Na–Sb alloy and an outer NaF cap.[14] XPS depth profiles verify the bilayer configuration with an inner Na–Sb alloy and an NaF-rich outer layer (Fig. 7e). The alloy layer enhances adhesion and lowers the nucleation barrier while the NaF cap suppresses electrolyte decomposition, producing a stable and flat Na||Na profile for more than 1000 h at 0.5 mA cm^{-2} (Fig. 7f). A $SnCl_2$ additive in carbonate electrolyte reacts spontaneously with Na metal to produce an inner Na–Sn alloy and outer NaCl-rich SEI. SEM and (energy dispersive X-ray) EDX mapping show uniform Na–Sn/NaCl deposition, and symmetric Na||Na cells display stable cycling beyond 500 h at 0.5 mA cm^{-2} with lower hysteresis (-Fig. 8a–f). In $Na_3V_2(PO_4)_3$ (NVP) full cells, this bilayer reduces interfacial impedance and improves rate capability (*e.g.*, ~101 mAh g^{-1} at 10 C) compared with blank electrolyte.[15] In contrast, the direct reaction of neat $SnCl_4$ with sodium produces a uniform Na–Sn alloy and NaCl-rich SEI. Optical photos and SEM imagery confirm this uniform morphology, showing a smooth electrode surface free of dendrites (Fig. 8g–i). This interphase sustains lifetimes of around 4500 h with hysteresis below 100 mV at 2 mA cm^{-2} and 3 mAh cm^{-2}, and about 1500 h at 5 mA cm^{-2} and 5 mAh cm^{-2}.[8] Symmetric cell cycling tests comparing $SnCl_4$, $SnCl_2$, and bare Na electrodes clearly demonstrate the superior stability of $SnCl_4$-derived SEI, which maintains stable voltage polarization (<100 mV) for over 4500 h at 2 mA cm^{-2} and 1 mAh cm^{-2}, whereas $SnCl_2$ and bare Na electrodes fail at ~1900 h and 1000 h, respectively (Fig. 8j).

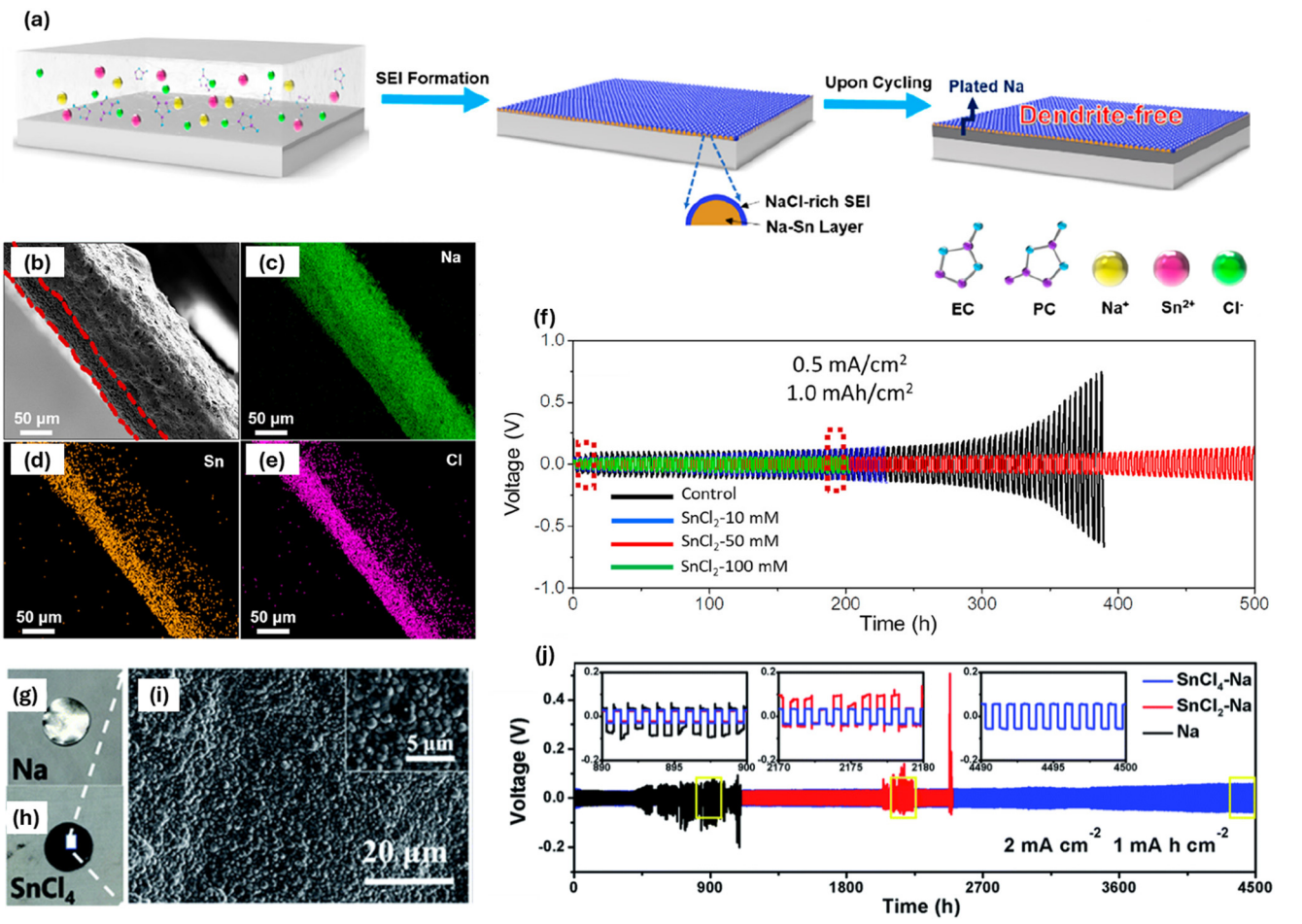

Fig. 8 (a) Fast and uniform ion transport from the *in situ* formed Na–Sn alloy layer plus NaCl-rich SEI, resulting in uniform plating–stripping and dendrite-free morphology. (b–e) Cross-sectional SEM and EDX mapping images of $SnCl_2$-treated Na metal with (c) Na, (d) Sn, and (e) Cl elemental signals. (f) Cycling performance of Na/Na symmetric cells with various concentrations of $SnCl_2$. Optical photos of (g) Na foil and (h) $SnCl_4$–Na electrode before cycling. (i) SEM image of the $SnCl_4$–Na electrode before cycling. (j) Cycling performance of symmetric cells with Na, $SnCl_4$–Na, and $SnCl_2$–Na electrodes at 2 mA cm^{-2} with cycling capacities of 1 mAh cm^{-2}.

Thus, while both $SnCl_2$ and $SnCl_4$ produce a Na–Sn/NaCl bilayer, the $SnCl_4$-derived SEI exhibits superior ionic conductivity and stability compared to $SnCl_2$, due to its uniform structure and higher Na^+ diffusion capabilities. This explains why the $SnCl_4$-based SEI can sustain longer cycling times and higher current densities. Because the 2 to 5 mA cm^{-2} current densities combined with 3 to 5 mAh cm^{-2} capacities exceed the threshold for fast charging in sodium metal cells, this system also serves as one of the most stringent fast charging benchmarks among halide derived interphases.

Rolling-assisted halide/alloy architectures are also effective. InF_3-assisted rolling produces a Na_2In (sodophilic) and NaF (stiff, ion-conductive) heterostructure throughout the bulk and surface, confirmed by XRD and XPS, and sustains >1100 h at 0.5 mA cm^{-2}/0.5 mAh cm^{-2} with reduced R_{SEI}/R_{ct} (Fig. 9a–d).[16] At solid-electrolyte interfaces, applying a spin-coated $BiCl_3$ and PTFE layer at the $Na_3Zr_2Si_2PO_{12}$ (NZSP)|Na contact creates a uniform and well-adhered artificial interphase. Cross-sectional SEM shows a dense and gap-free coating ~1.67 μm thick, with energy dispersive spectroscopy (EDS) mapping confirming the homogeneous distribution of the precursor components (Fig. 9e and f). Upon cycling, this layer yields a multifunctional Na_xBi (fast Na^+ path) + NaCl (wide bandgap) interphase that dramatically improves wetting and blocks electron injection. The Na/$BiCl_3$@NZSP/Na symmetric cell drops interfacial resistance from ~1252 to ~68 Ω and cycles ~3000 h at 0.1 mA cm^{-2} with a CCD of 2 mA cm^{-2} (Fig. 9g).[18] With appropriate control of thickness and uniformity, these alloy-underlayer/halide-cap designs suppress current focusing and extend to ≥5 mA cm^{-2} operation.

Chalcogenide based artificial interphases comprise two complementary families within the same group. Oxygen based oxides act as ultrathin passivation layers that provide strong electronic insulation and chemical stability, whereas sulfur and selenium based compounds furnish fast Na^+ pathways and, in combination with alloys, improve adhesion and compliance.[1] Their electronic structures provide suitable bandgaps that limit electron leakage while maintaining facile Na^+ migration.[1] Conformal Al_2O_3 deposited by *ex situ* ALD establishes a quantitative benchmark for ultrathin passivation (Fig. 10a). Films of ~1.4, 3.5, and 7 nm corresponding to 10, 25, and 50 cycles have been examined. The 25 cycle coating maintains an initial overpotential near 20 mV at 3 mA cm^{-2} and 1 mAh cm^{-2} and remains near 17 mV after 100 cycles, whereas bare sodium exceeds 50 mV with early soft shorting.[1] At 5 mA cm^{-2} the overpotential increases only from about 38 mV initially to about 40 mV after 100 cycles (Fig. 10b), and at 10 mA cm^{-2} the coating

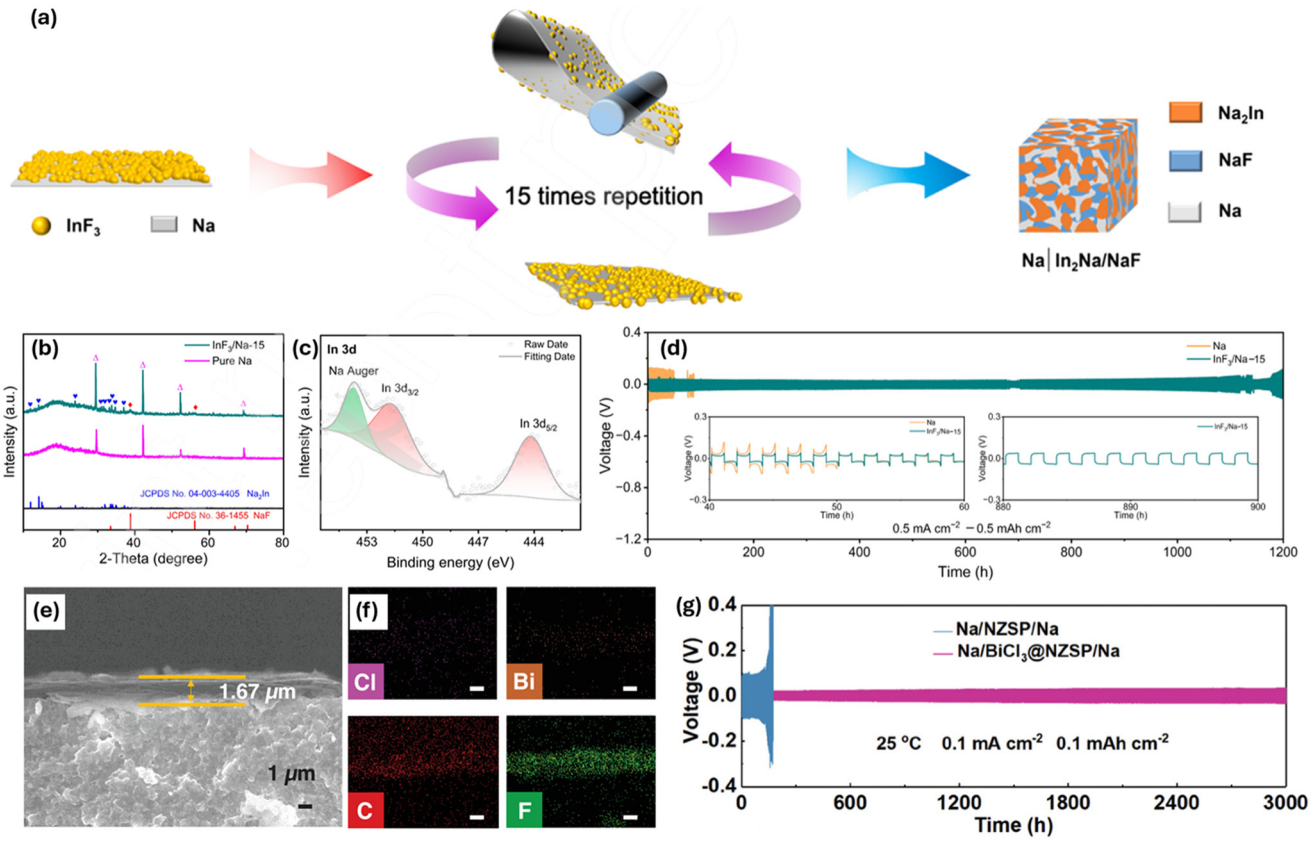

Fig. 9 (a) Flow chart of preparing sodium metal anodes modified by Na_2In/NaF biphase composite. (b) XRD patterns of InF_3/NaF and pure Na. (c) High-resolution XPS spectra of InF_3/NaF surface layer (In 3d). (d) Voltage–time curves of InF_3/Na and Na in symmetric cell at 0.5 mA cm^{-2}/0.5 mAh cm^{-2}. (e) Sectional SEM and corresponding (f) EDS mapping images of $BiCl_3$@NZSP pellet. (g) Voltage–time curves of Na/NZSP/Na and Na/$BiCl_3$@NZSP/Na symmetric cells at 0.1 mA cm^{-2}/0.1 mAh cm^{-2}.

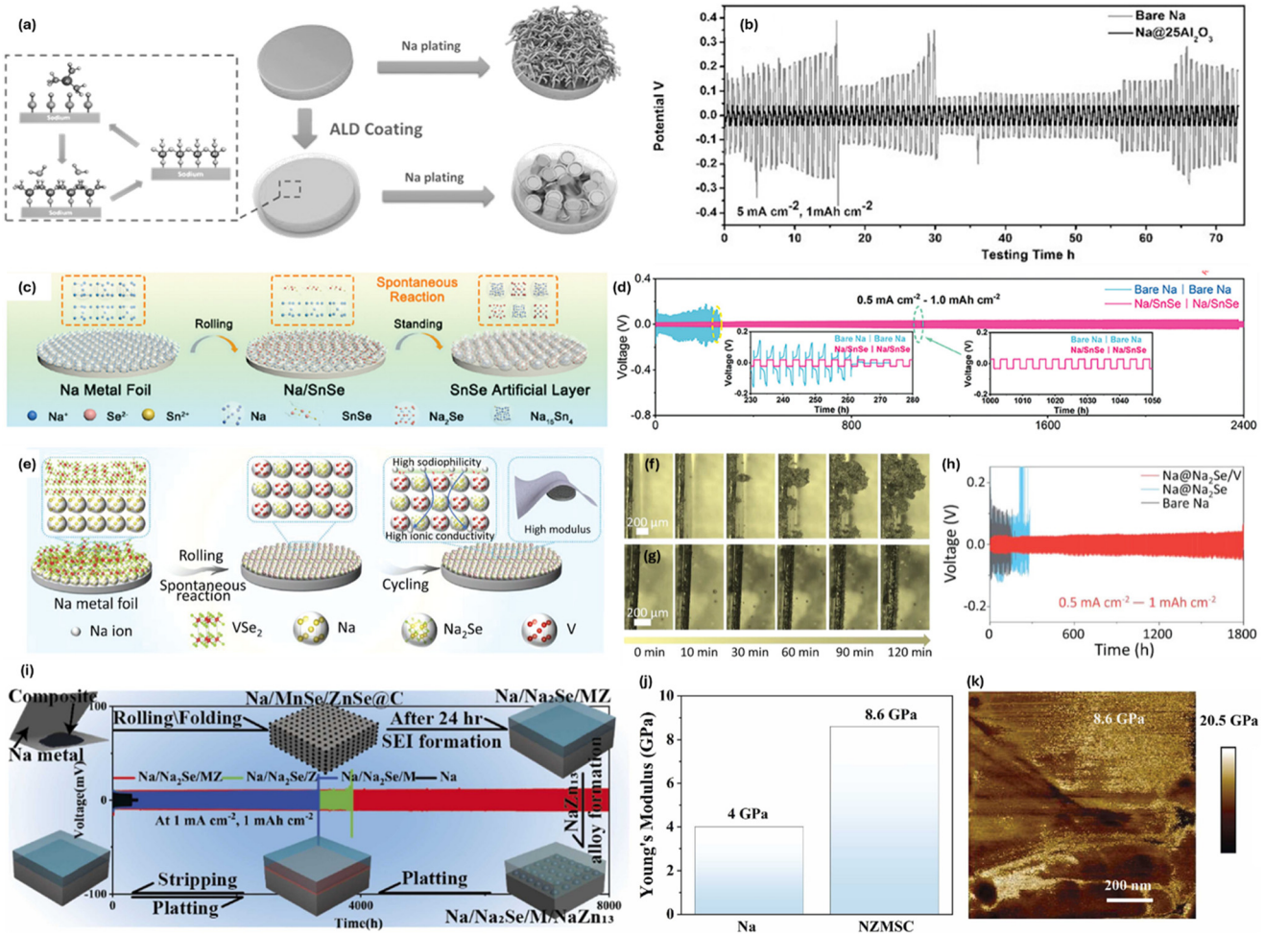

Fig. 10 (a) Schematic diagrams of Na stripping/plating on bare Na foil and Na foil with ALD coating. (b) Comparison of the cycling stability of the Na@25Al_2O_3 and the bare Na foil at a current density of 5 mA cm^{-2}. (c) Schematic image showing the synthesis process of Na/SnSe electrode. (d) Cycle performances at 0.5 mA cm^{-2}, 1.0 mAh cm^{-2}. (e) Schematic illustration of preparation of artificial heterogeneous Na_2Se/V interphase and its advantages. (f and g) Optical images of bare Na (f) and Na@Na_2Se/V (g) electrodes during the Na^+ plating process at 0.5 mA cm^{-2}. (h) Galvanostatic plating/stripping (0.5 mA cm^{-2}/1 mAh cm^{-2}). (i) Schematic of the *in situ* formation of the NZMSC interphase and its long-term galvanostatic cycling performance in a symmetric cell at 1 mA cm^{-2}, compared with other interphase compositions. (j) Comparison of Young's modulus between bare Na and the NZMSC surface and (k) corresponding AFM modulus map of the composite interphase.

sustains roughly 150 cycles. At 3 mA cm^{-2} the stripping and plating profile remains nearly unchanged for at least 500 cycles with flat plateaus. These 3 to 10 mA cm^{-2} current densities and 1 mAh cm^{-2} areal capacities fall squarely within the fast charging window as defined above, so this ultrathin oxide coating provides a direct benchmark for inorganic passivation under genuine fast charging conditions. Cracking observed under repeated plating and stripping is attributed to limited fracture toughness of Al_2O_3 and stress accumulation at the Na|Al_2O_3 interface due to cyclic volume change of Na during plating/stripping and severe elastic mismatch between Na and Al_2O_3.

Sulfur- and selenium-based interphases show greater crack tolerance and higher Na^+ conductivity, which mitigates fracture-driven degradation and relieves interfacial transport bottlenecks. Rolling SnSe nanoflakes onto sodium produces a Na_2Se and $Na_{15}Sn_4$ heterostructure (Fig. 10c) in which the Na_2Se outer layer supplies rapid Na^+ pathways and the $Na_{15}Sn_4$ inner alloy lowers the nucleation barrier and accommodates interfacial strain. Na||Na symmetric cells with this interphase operate for more than 2400 h at 0.5 mA cm^{-2} and 1 mAh cm^{-2} with very low hysteresis (Fig. 10d), and summaries around 1 mA cm^{-2} indicate ~1000 hour longevity for dual phase Na_2Se plus $Na_{15}Sn_4$ designs, consistent with uniform deposition and stress dissipation.[9] A related strategy employs a heterogeneous Na_2Se/V interphase, formed *in situ* by rolling a VSe_2 precursor onto the sodium metal (Fig. 10e).[19] The success of this composite relies on a synergistic mechanism elucidated by DFT calculations. The design leverages the high sodiophilicity of the metallic vanadium component (Na^+ adsorption energy of −2.128 eV *vs.* −1.100 eV on bare Na) to guide uniform Na^+ adsorption and prevent unwanted nucleation. Simultaneously, the Na_2Se phase acts as a superionic conductor, providing a low-energy pathway for rapid ion transport to the anode (diffusion barrier of 0.489

eV for Na_2Se and 0.772 eV for NaF). The effectiveness of this dendrite-suppression mechanism is visually confirmed through optical microscopy, which shows the modified electrode surface remaining sleek and uniform during plating, in stark contrast to the mossy, dendritic growth observed on bare sodium (Fig. 10f, and g). This combination of guided adsorption and fast transport results in high stability, demonstrating ~1790 h of symmetric cell cycling at 0.5 mA cm^{-2} and 1 mAh cm^{-2} (Fig. 10h) and more than 1800 cycles at 5 C in full cells. A multiphase strategy creates a Na_2Se/Mn/Zn composite (NZMSC) interphase by rolling a MnSe/ZnSe@C precursor with sodium, leveraging a three-part synergistic mechanism.[20] Manganese enhances the mechanical integrity of the layer, evidenced by an increased Young's modulus of ~8.6 GPa (more than double that of bare sodium as shown in Fig. 10j and k) and by the uniformly high local modulus in the AFM map of the composite interphase (Fig. 10k). Concurrently, zinc forms sodiophilic $NaZn_{13}$ alloy sites during the initial plating process, which guide uniform nucleation and suppress dendrites. This occurs while the Na_2Se matrix preserves a network for fast Na^+ transport. This robust, multifunctional design enables exceptional stability, with symmetric cells operating for an unprecedented 8000 h at 1 mA cm^{-2} and full cells cycling for over 2300 cycles at a high rate of 15 C.

Pnictide based interphases offer a compelling solution to the trade-off between mechanical stiffness and ionic transport, making them highly effective in stabilizing fast cycling. Although native interphases based on Na_2O and NaF can exhibit appreciable strength, *ex situ* strategies that introduce robust nitride or phosphide components can further stabilize high rate operation. For example, a mechanically kneaded and rolled Na and $NaNO_3$ composite anode bypasses the low solubility of nitrate additives by incorporating them directly into the anode (Fig. 11a).[21] This process produces a surface interphase containing ionically conductive NaN_xO_y and Na_3N species that promote uniform plating, in contrast to the dendritic growth on bare sodium. The resulting composite, ~400 μm thick, also exhibits significantly improved processability as it is less sticky and easier to handle than pure sodium. In Na||Na symmetric cells, this engineered interphase supports stable cycling for more than 600 h at 0.5 mA cm^{-2} and 0.5 mAh cm^{-2}, markedly outperforming the native interphase (Fig. 11b). Similarly, rolling red phosphorus onto sodium forms a Na_3P interphase that intrinsically combines exceptional mechanical strength with high ionic conductivity (Fig. 11c).[22] Atomic force microscopy (AFM) indentation measurements give a Young's modulus around 8.6 GPa compared with about 3.4 GPa for sodium (Fig. 11d). This mechanical robustness is complemented by excellent Na^+ transport, characterized by a high ionic conductivity of about 0.12 mS cm^{-1} and a remarkably low activation energy near 11 kJ mol^{-1} (Fig. 11e). Cryo-TEM imaging further confirms that the Na_3P layer promotes dense, dendrite-free deposition. As a result, in Na||Na cells this interphase maintains a flat voltage profile near 80 mV for about 780 h at 1 mA cm^{-2} and 1 mAh cm^{-2} (Fig. 11f). These pnictide-based examples thus highlight a key strategy that involves developing materials like Na_3P, which are intrinsically both mechanically robust and highly ionically conductive, thereby combining critical functions into a single, effective protective layer.

Combinations that integrate halide, chalcogenide, and pnictide functions in a single interphase co-optimize electron blocking, Na^+ conduction, and mechanical rigidity. For instance, a room-temperature reduction of an oxyhalide like BiOCl yields a Na_3Bi and Na_3OCl hybrid interphase (Fig. 12a).[23] This design leverages the high Young's modulus of the Na_3OCl component (~9.4 GPa, ~three times that of sodium) to physically suppress dendrites (Fig. 12b), which improves mechanical stability. DFT calculations indicate that Na_3OCl suppresses electron tunneling through its large bandgap while the Na_3Bi alloy phase tunes interfacial conductivity, and both phases possess low Na^+ migration barriers that guide uniform deposition beneath the interphase. Roll pressing BiOCl with sodium, which forms this composite layer, enables stable symmetric cell cycling for about 700 h at 1 mA cm^{-2} (Fig. 12c).[80] Another approach is a Na/VN-S composite prepared by *ex situ* pretreatment using VN, V, and Na_2S powders. This layer provides high sodiophilicity and stiffness together with a low nucleation barrier and a significantly reduced activation energy for Na^+ transport (E_a ~ 37 kJ mol^{-1}) (Fig. 12d). Na||Na symmetric cells with this interphase show stable cycling for more than 700 h at 1 mA cm^{-2} (Fig. 12e), and microscopy confirms uniform Na^+ transport without dendrites. A third strategy involves the immersion and rolling of sodium in PBr_3 in DME, which forms a NaBrP interphase in which Na_3P, NaBr, and Na_3PO_4 coexist.[81] This hybrid layer functions through a sophisticated synergistic mechanism: NaBr provides a low surface diffusion barrier for lateral Na^+ distribution, while Na_3P offers fast bulk permeation pathways through the layer, leading to uniform, columnar deposition (Fig. 12f). Electron microscopy reveals crystalline Na_3P and NaBr with Na_3PO_4, and the interphase supports dense metal deposition at 5 mAh cm^{-2} and more than 700 h at 1 mA cm^{-2} and 1 mAh cm^{-2} in symmetric cells (Fig. 12g).

In summary of section 4.1, inorganic *ex situ* artificial interphases are designed by balancing electron blocking with Na^+ transport, rigidity with compliance, thickness with defect control, adhesion with interfacial chemistry, and performance with scalable processing. Halide layers limit electron leakage and arrest cracks but, because of diffusion barriers and brittleness, are most effective as ultrathin films or as halide caps over sodiophilic alloys. Chalcogenide interphases deliver rapid transport yet benefit from alloy or oxide partners to address adhesion and durability. Oxide layers passivate effectively at nanometer thickness but crack more readily when used alone, which motivates hybridization with compliant phases. Pnictide based interphases combine conductivity and stiffness for long lived, low hysteresis cycling. Scalable routes including solution immersion with SbF_3, SnF_2, and $SnCl_2$, chemical conversion with $SnCl_4$, powder lamination, mechanical rolling including InF_3 assisted methods, and targeted interfacial coatings such as $BiCl_3$ with PTFE already deliver flat voltage profiles, low overpotentials, and efficiencies above 99% at current

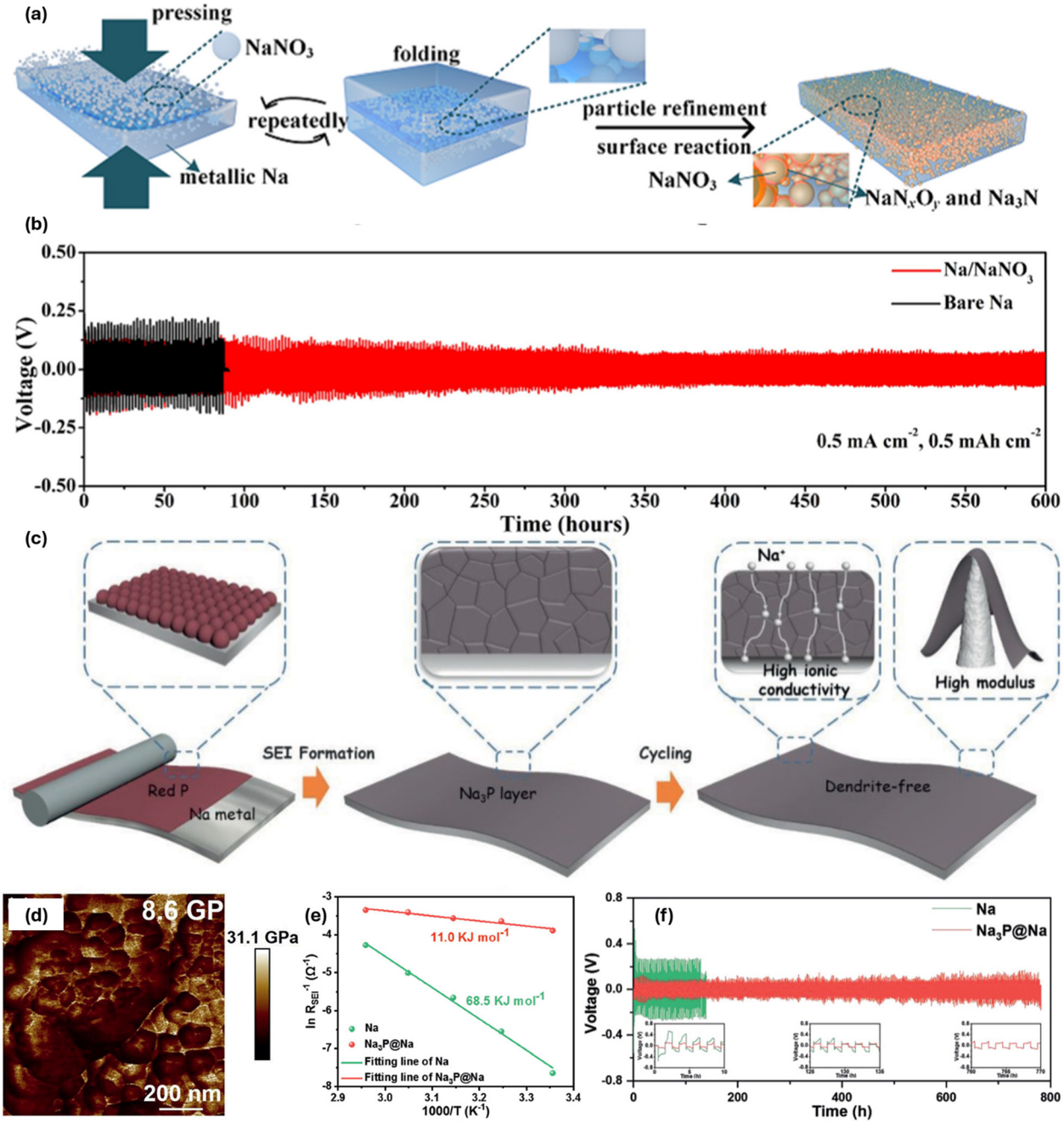

Fig. 11 (a) Schematic diagram of the fabrication of the $Na/NaNO_3$ composite foil *via* a mechanical kneading route with repeated folding and calendering. (b) Electrochemical comparison: voltage profiles of $Na/NaNO_3$||$Na/NaNO_3$ and Na||Na symmetric cells cycled at 0.5 mA cm^{-2} and 0.5 mAh cm^{-2}. (c) Schematic illustration showing how a Na_3P protective layer regulates Na^+ plating/stripping. (d) Surface Young's modulus map of Na_3P@Na anodes. (e) Activation energy (E_a) for Na^+ diffusion through the SEI layer. (f) Cycling performance of Na||Na and Na_3P@Na||Na_3P@Na symmetric cells at 1.0 mA cm^{-2} and 1.0 mAh cm^{-2} (insets: representative voltage profiles).

densities of 0.5 to 3 mA cm^{-2} and capacities of 0.5 to 3 mAh cm^{-2}. Within this landscape, most halide based interphases have so far been tested primarily at moderate currents around 0.25 to 1 mA cm^{-2}, whereas multiphase chalcogenide, pnictide, and oxide based designs that sustain 2 to 5 mA cm^{-2} at areal capacities near 2 to 5 mAh cm^{-2} represent genuine fast charging benchmarks for inorganic *ex situ* coatings.

In the future, nanometer level control of layer thickness, composition, and defects, together with surface alloying to reduce desolvation barriers, field homogenizing stacks that separate electron blocking and ion conduction, and viscoelastic sublayers for stress accommodation, implemented with roll to roll compatible processes and guided by *in situ* diagnostics and data driven design, will be central to stabilizing high rate sodium metal batteries.

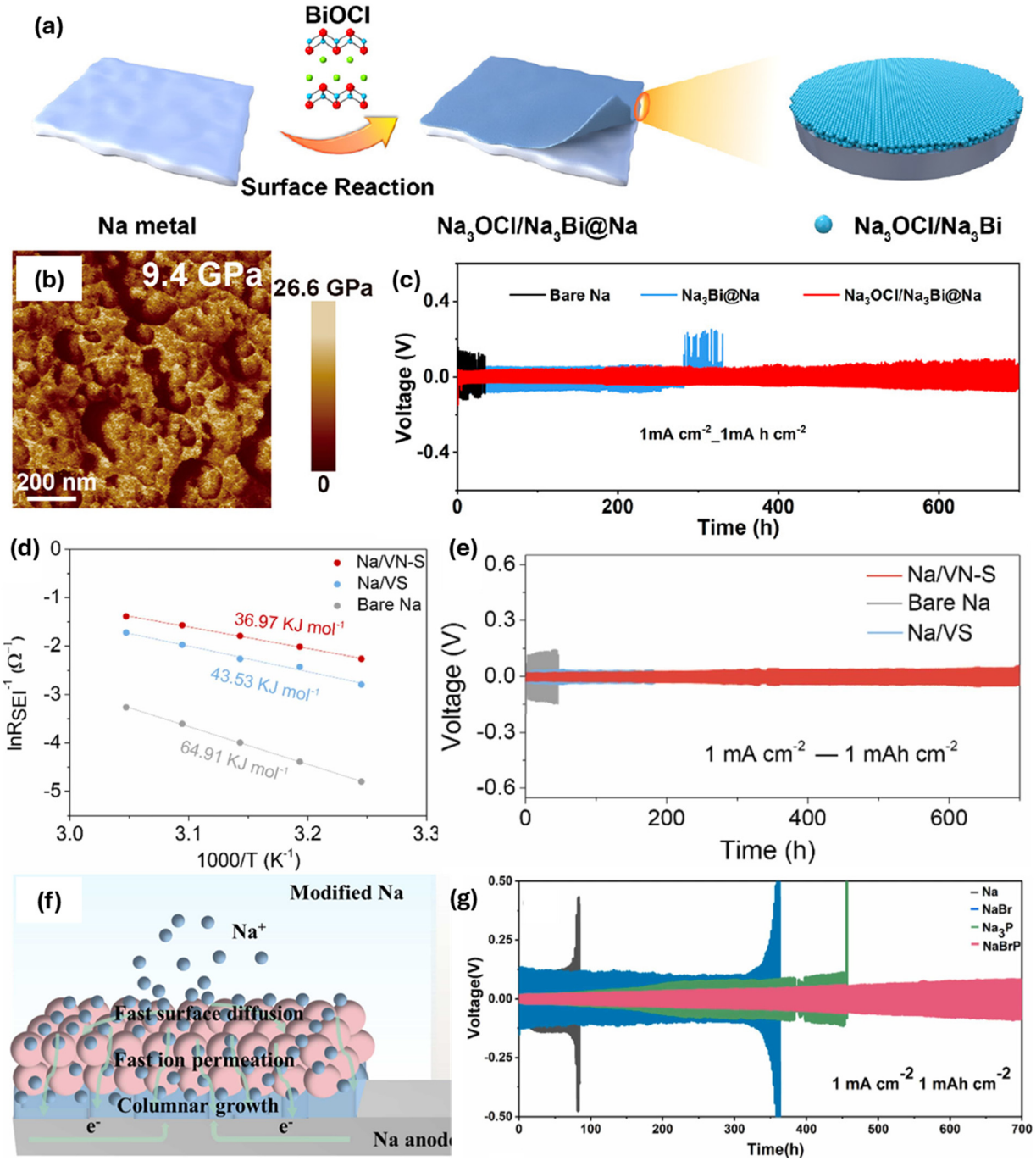

Fig. 12 Design and performance of multiphase inorganic interphases combining halide, chalcogenide, and pnictide functions. (a) Schematic of the *in situ* formation, (b) AFM modulus map, and (c) symmetric cell cycling performance (1 mA cm^{-2}) of a Na_3Bi/Na_3OCl hybrid interphase. (d) Arrhenius plot showing the activation energy for Na^+ transport and (e) galvanostatic cycling profile (1 mA cm^{-2}) for a Na/VN-S composite. (f) Schematic illustrating the synergistic surface/bulk ion transport mechanism and (g) symmetric cell cycling performance (1 mA cm^{-2}) for a NaBrP interphase.

4.2. Organic *ex situ* artificial interphase for fast charging and discharging

Organic aSEIs offer superior flexibility and stress-dissipation capabilities compared to their inorganic counterparts, making them advantageous for accommodating the volume changes that occur during plating and stripping and for maintaining uniform current distribution. By contrast, single-layer inorganic films often suffer from repeated Na plating/stripping induces interfacial voids/defects, leading them to be susceptible to cracking.[82]

These ionic conductive organic films are typically designed based on (1)chemically stable backbones that passivate Na and suppress further electrolyte decomposition, (2) polar functional groups that promote the desolvation of Na^+, and (3) long, flexible chains that provide pathways for

ion migration.[83] Consequently, they play a critical role in limiting the increase of SEI thickness and maintaining a uniform frontal film under high-rate conditions. Nevertheless, because organic films alone can lack the electron-blocking strength and stiffness sometimes required, hybridizing with alloy/inorganic components is used to combine high Na^+ conductivity with low electronic conductivity and robust mechanical integrity.[82]

Sulfur-rich polymer films represent a prominent example of organic *ex situ* aSEIs. Specifically, a poly(phenylene sulfide) (PPS) film can be created by immersing a sodium metal electrode in a THF solution containing *para*-dichlorobenzene and sulfur (Fig. 13a).[84] During initial cycling, the PPS-rich layer converts into a sodium benzenedithiolate (PhS_2Na_2)-rich protective layer. SEM analysis revealed that a uniform layer of ~5 μm was formed, extending the plating and stripping lifespan to about 800 h at a current density of 1 mA cm^{-2} and a capacity of 1 mAh cm^{-2} (Fig. 13b). This interphase maintained a uniform current distribution, thereby suppressing surface roughening. According to DFT calculations, the Na^+ binding energy of the PhS_2Na_2 protective layer is significantly lower than that of native SEI components like CH_3ONa and Na_2CO_3, which reduces the activation energy required for ion migration. Thus, the PPS-derived film achieves a balance between electron blocking and ion conduction due to its low electronic conductivity and high Na^+ affinity, while also ensuring compliance against cracking.

To simultaneously enhance mechanical stability and ionic conduction, protective films using polyvinylidene fluoride (PVDF) have been developed.[85] For instance, an *ex situ* SEI can be formed by coating a PVDF layer onto a copper current collector through doctor blading, followed by sodium plating. The stability of this interphase stems from a defluorination reaction between PVDF and sodium, which forms a composite SEI containing inorganic NaF (enabling fast Na^+ migration) and Na_2O_2 (providing a high shear modulus). This dual structure prevents electron leakage while allowing Na^+ to pass smoothly through the matrix, achieving a long cycle life of over 1200 h at 1 mA cm^{-2} and maintaining stability for ~900 h even at a higher rate of 2 mA cm^{-2} (Fig. 13c). In half-cell evaluations, the PVDF@Cu electrode maintained a high average CE of over 99.91% for 2000 h at 1 mA cm^{-2} and sustained a CE of 99.48% for over 1000 cycles at 2 mA cm^{-2} (Fig. 13d). These results signify that the PVDF-derived film provides both a high Young's modulus and flexibility, enabling it to dissipate stress without cracking.

An *ex situ* coating using the polymerization of 1,3-dioxolane (DOL) is a classic example of an organic film, where a thin and uniform poly(DOL) layer can be formed through a simple immersion process (Fig. 13e).[77] Lu *et al.* induced spontaneous polymerization on the surface by immersing sodium electrodes in a DOL solution for a matter of minutes, resulting in the formation of a homogeneous poly(DOL) film. This layer promotes Na^+ desolvation, blocks electronic conductivity, and absorbs repeated volume changes through its intrinsic flexibility, which was also shown to suppress gas evolution. Thanks to these properties, the poly(DOL)-treated electrode recorded a breakthrough lifespan of over 2800 h at 1 mA cm^{-2} with an overpotential of about 25 mV, and demonstrated significant stability even at 3 mA cm^{-2}, sustaining a flat voltage profile for over 130 h (Fig. 13f). The viscoelasticity of the organic polymer suppresses crack propagation by stretching or compressing in response to mechanical stress.

Another polymer protection approach involves the solid–gas reaction of formic acid vapor with the sodium surface to form a dense sodium formate (HCOONa) layer.[86] The HCOONa layer is denser and has higher mechanical strength than the native SEI, with a thickness of only ~0.65 μm (Fig. 13g). This rigid ionic lattice provides both electron blocking and Na^+ conduction and effectively prevents dendrite penetration due to its higher Young's modulus. The HCOONa@Na interphase achieved a long lifespan of about 2200 h in a diglyme-based electrolyte at a high current density of 2 mA cm^{-2} and 1 mAh cm^{-2} (Fig. 13h). These operating conditions lie within the fast charging regime for sodium metal, so the extended lifetime of the sodium formate interphase directly demonstrates that a thin, mechanically robust inorganic salt layer can withstand repeated high rate transients. Based on this success, recent studies have applied this interphase to anode-free sodium batteries. Since HCOONa is synthesized *via* a relatively simple and scalable solid–gas reaction, it can be safely applied in commercial cell fabrication.

The design of organic *ex situ* aSEIs also includes composite films that incorporate carbon or metal oxides within various porous structures. For example, an electrode can be fabricated by slurry-coating pre-synthesized zinc-doped hollow carbon nanotubes (Zn-HCNT).[87] In this design, the hollow nanotubes act as physical containers for sodium. Crucially, single-atom Zn sites on the inner wall serve as sodiophilic centers that guide Na nucleation and growth to occur preferentially inside the tubes through a mechanism known as encapsulation-based storage (Fig. 14a). This physical confinement of the deposited metal prevents dendrite formation on the exterior surface. Such an electrode maintained a lifespan of over 1000 h at a high rate of 5 mA cm^{-2} and over 900 h at an even higher rate of 10 mA cm^{-2} (Fig. 14b). The inset shows the magnified voltage profile from 775 to 776 h. These 5 to 10 mA cm^{-2} current densities are among the highest reported for sodium metal symmetric cells and clearly satisfy the fast charging conditions for sodium metal anodes. Similarly, slurry-coating metal–organic framework (MOF-199) particles onto a current collector provides a tunable porous framework.[88] This layer acts as a robust physical shield that serves as a buffer for Na deposition, preventing the deposited metal from penetrating the separator, a failure mode observed on pristine Cu electrodes (Fig. 14c). When applied to sodium anodes in a carbonate electrolyte, the MOF-199 layer improved the initial CE from ~60 to ~77% and maintained it for 26 cycles at 1 mA cm^{-2}, whereas the unprotected anode failed after only 10 cycles (Fig. 14d). Bio-material-based organic films, such as a thin (~100 nm) pyroprotein seed layer (PSL) (Fig. 14e)[89] or a free-standing N-doped mesoporous carbon paper (CPPY) (Fig. 14f),[90] are used as coatings or hosts to increase sodiophilicity. The PSL acts as a catalytic seed layer with numerous nucleophilic active

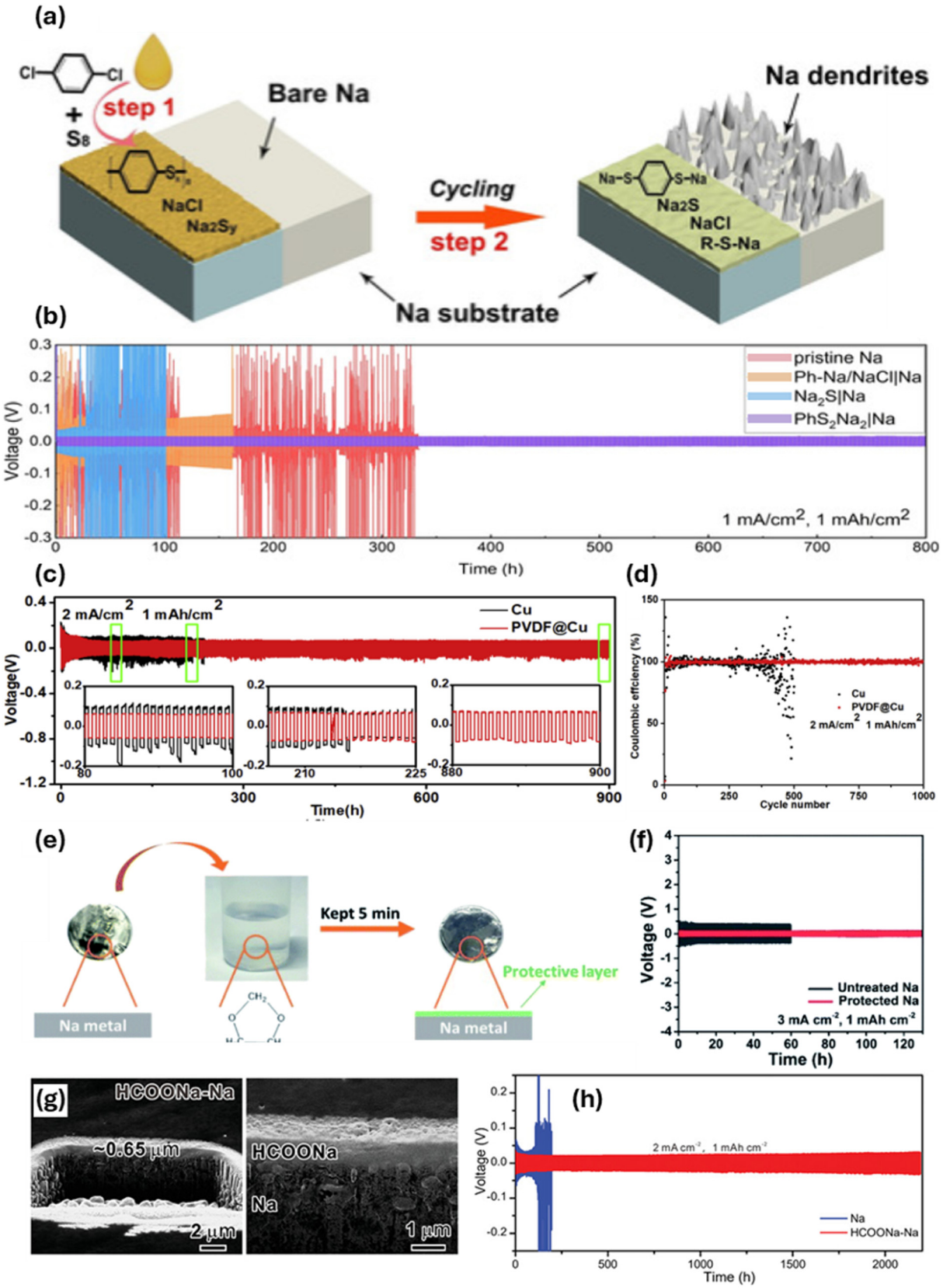

Fig. 13 (a) Schematic of the fabrication process for a poly(phenylene sulfide) (PPS)-derived interphase. The blue color of the Na substrate is used to schematically distinguish the protected electrode region from the pristine bare sodium (gray). (b) Long-term galvanostatic cycling of the resulting PhS_2Na_2-protected symmetric cell at 1 mA cm^{-2}. (c) High-rate cycling performance of a PVDF-coated symmetric cell at 2 mA cm^{-2}. (d) Corresponding CE of the PVDF-coated cell at 2 mA cm^{-2}. (e) Schematic showing the formation of a poly(DOL) layer *via* simple immersion. (f) High-rate cycling stability of the poly(DOL)-protected cell at 3 mA cm^{-2}. (g) Cross-sectional FIB- helium ion microscopy (HIM) image showing the thin, dense sodium formate (HCOONa) interphase. (h) Long-term cycling performance of the HCOONa-protected symmetric cell at 2 mA cm^{-2}.

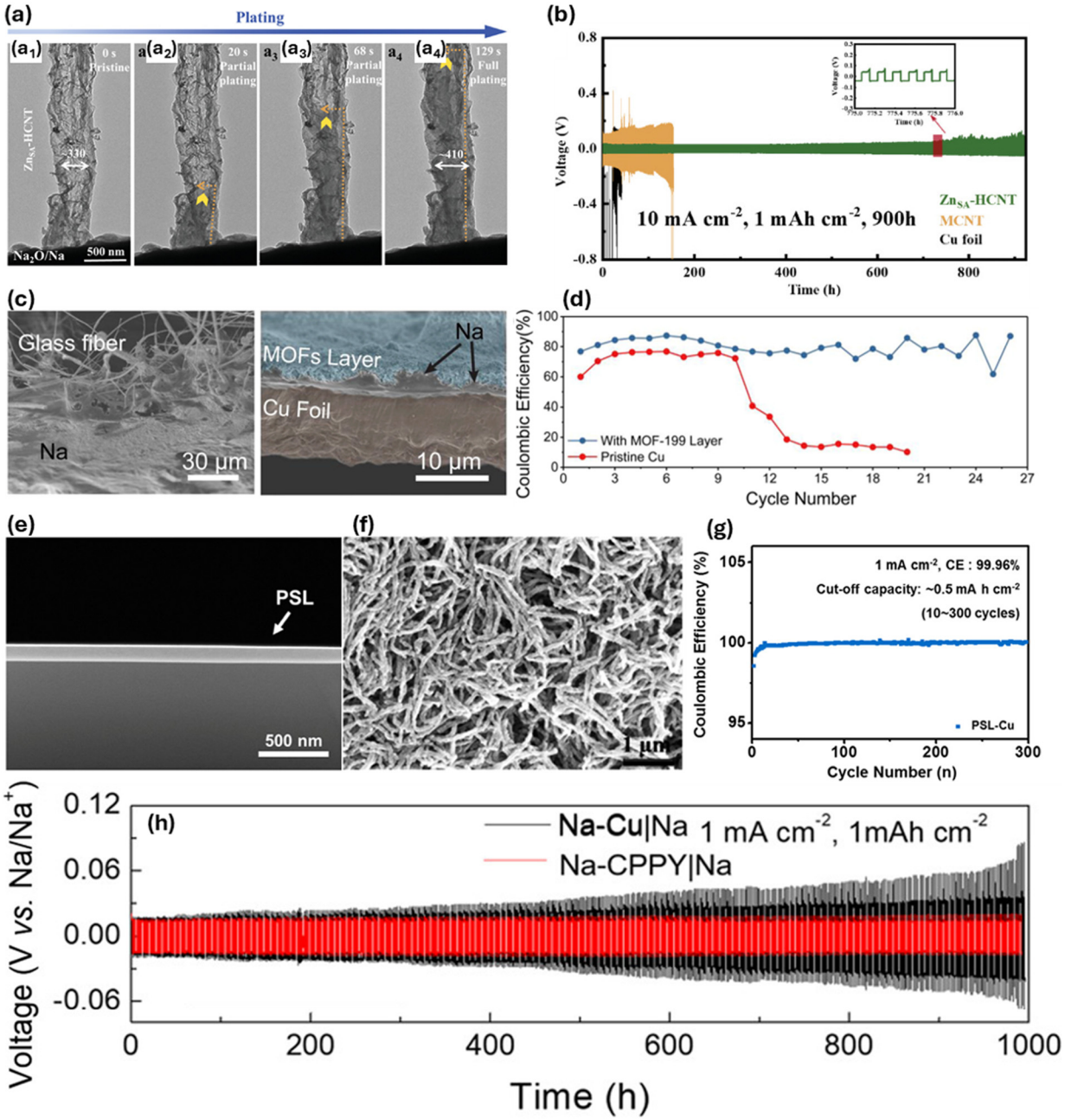

Fig. 14 (a) *In situ* TEM sequence (a1–a4) showing the encapsulation of Na metal, from the pristine state (a1) to being partially (a2 and a3) and fully filled (a4), inside a Zn-doped hollow carbon nanotube (ZnSA-HCNT). (b) Long-term, high-rate cycling performance of the ZnSA-HCNT symmetric cell at 5 mA cm^{-2}. The inset displays the magnified voltage profiles from 775 to 776 h. (c) Cross-sectional SEM images comparing Na deposition on bare Cu (top) *versus* a MOF-199 coated electrode (bottom), where the MOF layer acts as a buffer. (d) Corresponding CE of the MOF-199 protected Na anode compared to an unprotected anode. (e) SEM image of a thin PSL on a current collector. (f) SEM image showing the porous, nanofibrillar structure of a free-standing CPPY. (g) Long-term cycling stability demonstrating the high CE of the PSL-coated anode. (h) Stable, long-term cycling of the CPPY symmetric cell at 1 mA cm^{-2}.

sites, guiding homogeneous Na deposition and maintaining a low nucleation overpotential even at 4 mA cm^{-2}. This results in a high mean CE of ~99.96% over 300 cycles at 1 mA cm^{-2} (Fig. 14g). The 3D porous CPPY network reduces the local current density and provides N-doped sodiophilic sites, enabling stable dendrite-free cycling for over 1000 h at 1 mA cm^{-2} (Fig. 14h) and showing stable performance at 2 mA cm^{-2}.

Summarizing section 4.2, various organic aSEIs hold a competitive edge in preprocessing and scalability. Poly(DOL) and PPS can be prepared by solution immersion, enabling the simultaneous treatment of many electrodes. PVDF coatings and NaF/C–F/C═C composite films can be applied to large-area electrodes through mechanical processes such as doctor blading or rolling. Ionic polymer films and

HCOONa layers can be produced at relatively low temperatures using gas–solid reactions or electrochemical polymerization, which is compatible with other battery components. Overall, organic films maintain a low thickness while increasing ionic conductivity, suppressing electronic conduction, and absorbing high compressive, tensile, and shear loads to preserve mechanical integrity during repeated plating and stripping. Even under current densities of 0.5 to 3 mA cm^{-2} and areal capacities of 0.5 to 3 mAh cm^{-2}, these designs have been reported to maintain low overpotentials of about 20 to 35 mV and high Coulombic efficiencies of 95 to 99.5%. Within this group poly(DOL) films, sodium formate interphases, and encapsulation based porous host architectures have been explicitly demonstrated at 2 mA cm^{-2} and above and therefore probe the fast charging regime, whereas most other organic coatings currently provide long lived benchmarks at moderate current densities near 0.5 to 1 mA cm^{-2}.

For the future advancement of organic aSEIs, molecular-level design and interfacial engineering are crucial. First, the desolvation barrier should be lowered and ion channels expanded by introducing polymer chains with functional groups such as ether, carbonate, and sulfonic acid that interact favorably with sodium ions. Second, cross-linking or polymer network formation can be used to minimize phase separation and enhance mechanical integrity. Third, hybridization with inorganic nanoparticles such as NaF, Al_2O_3, and Na_3P should be employed to increase electron-blocking capability and tensile strength, with surface functionalization that ensures strong bonding to the polymer. Finally, industrially scalable techniques such as roll-to-roll coating, solution injection, and spray coating should be adopted to ensure uniform thickness and composition over large-area electrodes. By implementing such multifunctional designs that simultaneously satisfy electron blocking, Na^+ conduction, mechanical rigidity, viscoelasticity, adhesion, and process efficiency, organic *ex situ* aSEIs can significantly enhance the stability and energy density of next-generation sodium metal batteries that require high-rate charging.

4.3. Hybrid *ex situ* artificial interphase for fast charging and discharging

Hybrid aSEIs, which concurrently embody the properties of both inorganic and organic layers, are effective for achieving uniform ion flux, high mechanical strength, electron blocking, and mechanical compliance in rapid sodium plating and stripping. Organic layers provide elasticity and viscoelastic dissipation that absorb repeated volume changes, whereas inorganic domains add wide bandgap insulation and a high modulus that suppress electron leakage and improve stability. However, single-component layers face intrinsic limitations: pure inorganic coatings are prone to brittle fracture under the large volume fluctuations of sodium metal, creating fresh crack sites for dendrite nucleation. Conversely, organic films often lack the sufficient shear modulus required to physically suppress dendrite propagation. The hybrid approach resolves these trade-offs by creating a synergistic composite where the organic phase acts as a viscoelastic buffer to dissipate localized mechanical stress, thereby preserving the structural integrity of the rigid inorganic domains. Simultaneously, the inorganic components provide the necessary mechanical strength and electronic insulation that soft polymers typically lack. Integrating these attributes in one interphase limits thickness growth and reduces cracking under high current densities.

Blade-coated fluorinated polymer and halide composites illustrate halogen-based hybrids prepared by solution processing. A NaF-PVDF (PNF) mixture cast on copper produces a smooth composite film where NaF microparticles are uniformly distributed within a viscoelastic PVDF matrix.[3] This design creates a synergistic soft-rigid protective layer. The flexible PVDF matrix accommodates volume changes during cycling, while the rigid NaF particles provide both high mechanical strength with a composite Young's modulus of ~7.43 GPa and fast Na^+ diffusion pathways. This synergistic design results in a smooth and dendrite-free surface. Specifically, SEM analysis after 100 cycles at 2 mA cm^{-2} shows the PNF@Cu anode remains flat and compact, a stark contrast to the rough, dendritic morphology of bare sodium under the same conditions (Fig. 15a and b). In Na||Na symmetric cells, the PNF@Cu interphase sustains stable cycling for ~500 h at a high rate of 5 mA cm^{-2} (Fig. 15c), outperforming PVDF-only coatings. A solvent-free solid-state route achieves a related inorganic–organic network by rolling PVDF powder with sodium (Fig. 15d), triggering an *in situ* reaction that generates a hybrid NaF and C–F/C=C network.[91] In this layer, the inorganic NaF provides high sodiophilicity and fast ion transport, characterized by a low activation energy of 39.1 kJ mol^{-1}, while the organic network offers toughness to accommodate mechanical stress. The PVDF-rolled sodium electrode exhibits excellent high-rate capability in full cells. When paired with $Na_3V_2(PO_4)_3$, it retains 85% of its capacity after 600 cycles at a high rate of 10 C (Fig. 15e) and remains stable across a wide temperature range from −40 to 55 °C.

Oxide–organic hybrids prepared by *ex situ* deposition provide nanometer-scale passivation and strong interfacial bonding while retaining ion transport. One approach is molecular layer deposition (MLD) of alucone on sodium at 85 °C using trimethylaluminum and ethylene glycol.[2] This process yields an adherent, flexible inorganic–organic coating with strong Na–O and Na–Al bonding that physically suppresses dendrite growth (Fig. 16a). With the cycle number tuned to 25, Na||Na cells maintain a flat profile for more than 270 h at 1 mA cm^{-2} and show stable cycling for over 100 h at a high rate of 3 mA cm^{-2}. Post-cycling SEM analysis confirms the effectiveness of this layer, showing a smooth and dendrite-free surface on the protected anode in stark contrast to the mossy, dendritic structure on bare sodium (Fig. 16b–e). MLD alucone is also mechanically distinct from brittle oxides: increasing the

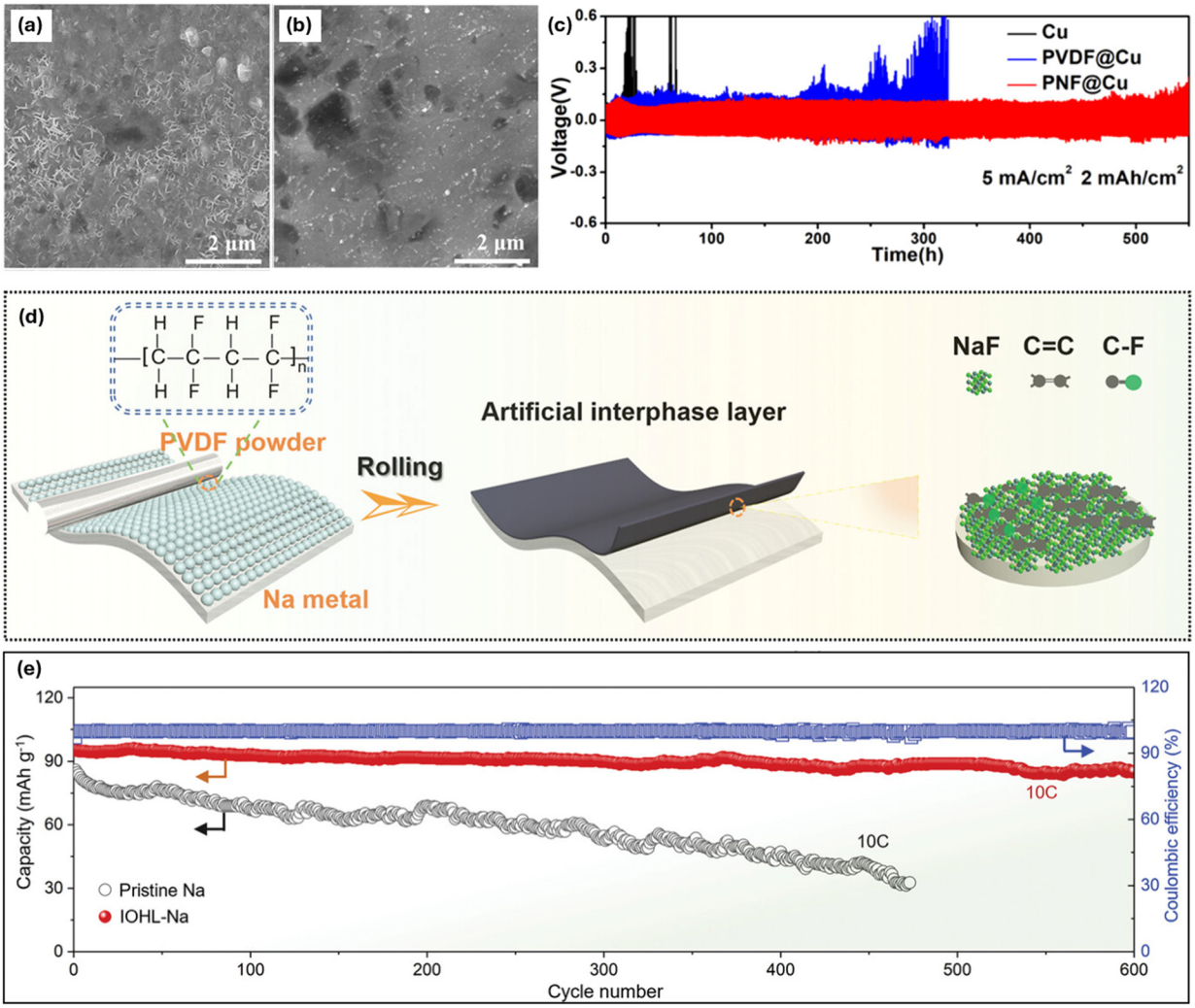

Fig. 15 (a and b) Comparison of surface morphology after 100 cycles at 2 mA cm^{-2} for (a) a bare sodium anode, showing dendritic growth, and (b) a PNF@Cu protected anode, showing a smooth, dendrite-free surface. (c) High-rate cycling stability of the PNF@Cu symmetric cell at 5 mA cm^{-2}. (d) Schematic of the formation of an *in situ* reacted IOHL-Na *via* rolling PVDF powder on sodium. (e) High-rate, long-term cycling performance of a full cell using the IOHL-Na anode at 10 C.

organic-chain length transforms the coating from brittle to ductile, reaching a crack-onset strain of ~9.9% and a reduced modulus of ~4.6 ± 2.1 GPa.[78] This ductility, combined with conformality, helps maintain interfacial contact during rapid plating/stripping while the inorganic component preserves electron blocking. Accordingly, ultra-thin Al_2O_3/alucone stacks act as passivating yet crack-tolerant layers under high-rate cycling. Stacking ALD Al_2O_3 with MLD alucone further refines adhesion and allows for the creation of nanolaminate or nanoalloy structures (Fig. 16f).[92] Among various architectures tested, a nanoalloy structure with alternating single layers of Al_2O_3 and alucone, noted as Na@$(1ALD\text{-}1MLD)_{10}$, demonstrated exceptional high-rate stability. This specimen maintained a low overpotential of about 30 mV for ~1500 h at a high rate of 3 mA cm^{-2} and 1 mAh cm^{-2} (Fig. 16g). Further insight into this stability is provided by cohesive-zone modeling, a simulation technique used to analyze the mechanical failure of the interphase. The model reveals that due to its larger molar volume, sodium exerts significantly lower mechanical stress on the protective layer during plating compared to lithium. This lower stress explains why a thin 4 nm layer is sufficient to stabilize sodium, whereas lithium's higher plating pressure requires a much thicker layer greater than 20 nm to prevent the interphase from cracking and delaminating.

Another strategy involves drop-casting a solution of $SnCl_2$ and 4-chloro-2,6-dimethylphenol onto the sodium surface to form an inorganic–organic hybrid layer (IOHL-Na) *in situ* (Fig. 16h).[93] This interphase integrates an inorganic stannide and NaCl with an aryl-based polymer, providing a high Young's modulus, strong chemical bonding, and flexible elasticity simultaneously. Consequently, IOHL-Na maintains a CE of 98.5% for 800 cycles at 2 mA cm^{-2}. In symmetric cells, it sustains an ultralong lifespan of more than 2000 h with an extremely low overpotential of 15.8 mV at a very high current density of 4 mA cm^{-2} and a large capacity of 4 mAh cm^{-2} (Fig. 16i). The insets display the magnified voltage profiles at

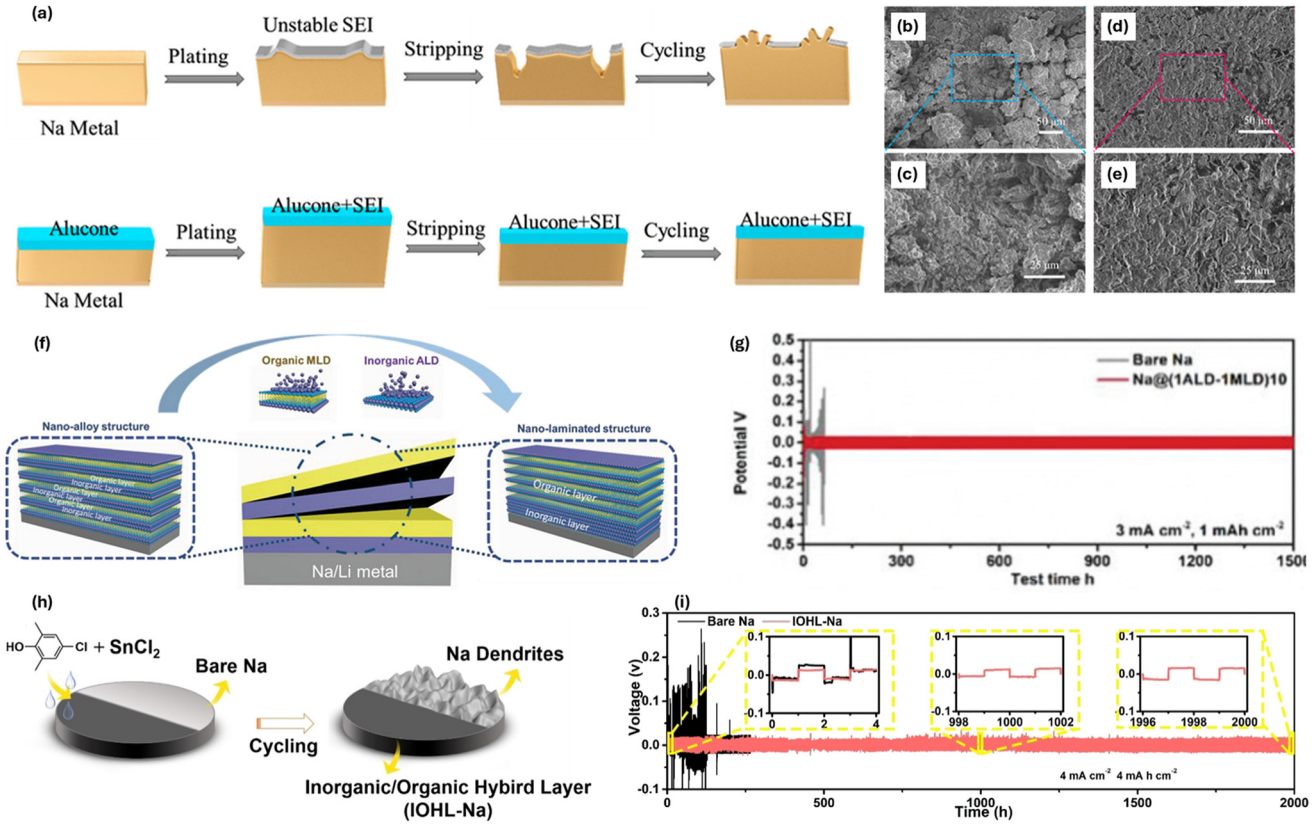

Fig. 16 (a) Schematic comparing Na plating/stripping on bare Na *versus* MLD alucone-coated Na. (b–e) Post-cycling top-view SEM images comparing the morphology of (b and c) bare Na, showing mossy and dendritic growth, with (d and e) Na@25Alucone, showing a smooth, uniform surface after 10 cycles at 1 mA cm^{-2}. (f) Schematic illustrating the fabrication of nanoalloy *versus* nano-laminated hybrid structures *via* ALD/MLD. (g) High-rate, long-term cycling stability of the optimized Na@$(1ALD\text{-}1MLD)_{10}$ nanoalloy interphase at 3 mA cm^{-2}. (h) Schematic of the *in situ* formation of IOHL-Na. (i) Galvanostatic cycling curves of the IOHL-Na symmetric cell at an ultra-high rate of 4 mA cm^{-2} and 4 mAh cm^{-2}. The insets display the magnified voltage profiles at the initial, middle, and final stages.

the initial, middle, and final stages. The inorganic component suppresses parasitic reactions, while the organic component prevents interfacial cracking. The combination of 4 mA cm^{-2} and 4 mAh cm^{-2} places this test firmly in the fast charging window and highlights that the hybrid interphase can maintain interfacial integrity under aggressive high flux conditions.

To summarize section 4.3, hybrid interphases resolve the tradeoff between electron blocking and Na^+ conduction while managing rigidity, compliance, thickness, and adhesion through combinations of ceramic and polymer phases. Halogen-based PVDF and NaF coatings deliver strain accommodation with embedded electron-blocking domains, solid-state PVDF rolling offers solvent-free processing and a wide temperature window, and chalcogen-based alucone and Al_2O_3 stacks provide high modulus and strong bonding at nanometer thickness. Solution-derived metal–organic hybrids such as IOHL-Na raise interfacial bonding while retaining elasticity. These materials maintain uniform ion flux, prevent current localization, and enable lifetimes from 500 to 2000 h with overpotentials near 15 to 30 mV and high CE in the 0.5 to 3 mA cm^{-2} and 0.5 to 3 mAh cm^{-2} regime. Among them PVDF NaF composites, nanoalloyed Al_2O_3 and alucone stacks, and IOHL Na stand out by sustaining 3 to 5 mA cm^{-2} at areal capacities up to 4 mAh cm^{-2}, thus meeting the fast charging criteria defined earlier, whereas many other hybrids are at present validated mainly around 1 mA cm^{-2} as durable moderate rate references.

In the future, progress will depend on precise control of hybrid composition and thickness using cycle-accurate MLD and ALD, tuning period and sequence in nanolaminates to optimize adhesion energy and crack deflection, solvent-free routes that disperse ceramic domains uniformly without forming electronic percolation, and graded interphases that vary modulus and ionic conductivity through the thickness to homogenize current density. Mechanically informed molecular design of polymer backbones and side chains that lower desolvation barriers while preserving segmental mobility, together with *in situ* mapping of stress and ion flux and data-guided optimization, will accelerate the development of ultrathin hybrids that deliver low hysteresis and long life at practical current and capacity levels.

5. Outlook

Sodium metal anodes, with their high theoretical capacity and low redox potential, remain one of the most promising candidates for the next generation of energy storage in large-

scale renewable integration. However, the inherent instability of sodium metal anode under fast charging and discharging, which manifests in dendritic growth, low CE, and fragile interphases, poses formidable challenges to practical deployment. In this review, we highlighted the unique failure mechanisms of sodium metal anodes under transient high-rate operation, discussed interphase construction strategies, and compared inorganic, organic, and hybrid artificial interphases. Building on these insights, several forward-looking directions can be envisioned.

First, mechanistic understanding of fast ion interfacial kinetics should be deepened. Advanced operando characterization techniques combined with computational simulations will be essential to disentangle the coupled processes of Na^+ migration, desolvation, diffusion across the SEI, and nucleation under large current fluxes. Such studies will help establish quantitative descriptors that can guide the design of the interphase under practical fast charging and discharging conditions. Quantitatively, bare sodium in conventional ether- and carbonate-based electrolytes generally shows limited stability: in Na||Na symmetric cells at modest current densities around 0.5–1 mA cm^{-2} and areal capacities near 1 mAh cm^{-2}, voltage hysteresis typically grows and dendrite-induced short-circuit events appear within only tens to on the order of a hundred hours. At higher current densities of several mA cm^{-2}, these signatures emerge even sooner and reversible operation is often confined to a few tens of hours, reflecting the narrow safe window of the native Na|electrolyte interface under fast-charging conditions.

Second, rational design of artificial interphases remains the most viable route to stabilize sodium metal anodes. Future work should emphasize multifunctional aSEI layers that balance ionic conductivity, mechanical robustness, and chemical stability. Importantly, other than composition design, structural design is also critical for fast charging and discharging. Hybrid inorganic/organic structures, gradient or multilayer architectures, and self-healing functionalities may provide durable protection against dendrites and interfacial fracture during rapid cycling.

Third, translating these interphase strategies to large-scale applications requires addressing several critical system-level considerations. The first of these is moving beyond Na||Na symmetric cells or half-cells. In a full-cell configuration, constraints from the cathode's areal capacity, electrode kinetics, practical electrolyte-to-capacity (E/C) ratios, and limited Na inventory introduce coupled challenges that can significantly tighten the operational window for fast charging. Therefore, future aSEI strategies must be validated not only for their intrinsic properties (CE, CCD) but also for their robustness in practical full cells using high-loading cathodes and lean electrolytes.

A critical and interconnected system-level metric is the N/P ratio. Many existing studies report apparently stable fast-charging data using thick Na foil, corresponding to a high N/P ratio ($N/P \gg 1$) where the irreversible loss of Na is masked by the vast excess. For practical energy density and cost, particularly in grid storage, the N/P ratio must be drastically reduced (*e.g.*, N/P ~3 or lower), necessitating the use of ultra-thin Na foil or Na-lean anodes.[86] In these Na-lean conditions, the tolerance for dead Na becomes near-zero. Any inefficiency, SEI growth, or gas evolution during fast charging directly consumes the limited Na inventory, leading to rapid cell failure. This demands an extremely high Coulombic efficiency (*e.g.*, >99.9%) during fast charging, a requirement that must be explicitly targeted by future interphase research, potentially by defining a 'practical low-N/P window' based on deposition/dissolution efficiencies.[94]

Fourth, scale-up and commercialization impose additional constraints that go beyond electrochemical metrics. While techniques like ALD/MLD offer exquisite nanoscale control, they face significant hurdles in throughput, cost, and large-area uniformity for roll-to-roll processing. Conversely, strategies based on solution immersion, doctor blading, rolling, or vapor treatment may be more readily integrated with existing Li-ion manufacturing lines, offering a more pragmatic path to scale-up. However, even with an ideal interphase, the lack of robust, scalable technology for producing ultra-thin sodium metal anodes remains a critical bottleneck.[44] Furthermore, scale-up introduces system-level issues such as gas management (swelling), module-level thermal management, separator wetting, and stack pressure, all of which interact with the interphase design and must be co-optimized for safe and reliable large-scale deployment.

Finally, artificial intelligence/machine learning-assisted materials discovery and multiscale modeling frameworks may accelerate the optimization of interphases and electrolytes. By integrating large datasets from experiments and simulations, predictive models can identify optimal chemistries and architectures for fast-charging sodium metal anodes with shortened development cycles.

In summary, while the fragility of sodium metal anodes under fast charging/discharging remains a key barrier, converging advances in interphase engineering, electrolyte optimization, *in situ* diagnostics, and scalable fabrication offer a clear pathway forward. With concerted efforts, it is anticipated that safe, durable, and high-rate sodium metal batteries will transition from laboratory concepts to practical solutions for large-scale renewable energy storage.

Conflicts of interest

The authors declare no conflict of interest.

Data availability

No primary research results, software or code have been included and no new data were generated or analysed as part of this review.

Acknowledgements

This work was mainly supported by the US National Science Foundation, Award number CBET-2207302. The authors also acknowledge the support from the KIAT GITCC program

(Award No. P0030256) by the Korea Ministry of Trade, Industry and Energy (MOTIE).

References

1 Y. Zhao, *et al.*, Superior stable and long life sodium metal anodes achieved by atomic layer deposition, *Adv. Mater.*, 2017, **29**(18), 1606663.
2 Y. Zhao, *et al.*, Inorganic–organic coating via molecular layer deposition enables long life sodium metal anode, *Nano Lett.*, 2017, **17**(9), 5653–5659.
3 Z. Hou, *et al.*, Hybrid protective layer for stable sodium metal anodes at high utilization, *ACS Appl. Mater. Interfaces*, 2019, **11**(41), 37693–37700.
4 Y. Zhang, *et al.*, Ultrahigh active material content and highly stable Ni-rich cathode leveraged by oxidative chemical vapor deposition, *Energy Storage Mater.*, 2022, **48**, 1–11.
5 Y. Zhang, *et al.*, Recent achievements toward the development of Ni-based layered oxide cathodes for fast-charging Li-ion batteries, *Nanoscale*, 2023, **15**(9), 4195–4218.
6 J. Newman and N. P. Balsara, *Electrochemical systems*, John Wiley & Sons, 2021.
7 C. Monroe and J. Newman, The impact of elastic deformation on deposition kinetics at lithium/polymer interfaces, *J. Electrochem. Soc.*, 2005, **152**(2), A396.
8 Q. Chen, *et al.*, Building an artificial solid electrolyte interphase with high-uniformity and fast ion diffusion for ultralong-life sodium metal anodes, *J. Mater. Chem. A*, 2020, **8**(32), 16232–16237.
9 L. Cao, *et al.*, A Rooted Multifunctional Heterogeneous Interphase Layer Enabled by Surface-Reconstruction for Highly Durable Sodium Metal Anodes, *Adv. Funct. Mater.*, 2024, **34**(18), 2313962.
10 S. Choudhury, *et al.*, Designing solid-liquid interphases for sodium batteries, *Nat. Commun.*, 2017, **8**(1), 1–10.
11 H. Tian, *et al.*, Ultra-stable sodium metal-iodine batteries enabled by an in-situ solid electrolyte interphase, *Nano Energy*, 2019, **57**, 692–702.
12 R. Damircheli, *et al.*, Fluorinated artificial solid–electrolyte–interphase layer for long-life sodium metal batteries, *ACS Appl. Mater. Interfaces*, 2023, **15**(47), 54915–54922.
13 M. Xu, *et al.*, NaF-rich solid electrolyte interphase for dendrite-free sodium metal batteries, *Energy Storage Mater.*, 2022, **44**, 477–486.
14 W. Fang, *et al.*, A bilayer interface formed in high concentration electrolyte with SbF3 additive for long-cycle and high-rate sodium metal battery, *J. Power Sources*, 2020, **455**, 227956.
15 X. Zheng, *et al.*, Toward a stable sodium metal anode in carbonate electrolyte: a compact, inorganic alloy interface, *J. Phys. Chem. Lett.*, 2019, **10**(4), 707–714.
16 J. Xie, In situ architecting Na2In/NaF heterostructure enabling integrated bulk-interface stabilization for long-cycling sodium metal batteries, *J. Alloys Compd.*, 2025, **1045**, 184751.
17 Y. Zhang, *et al.*, Electrode architecture design for fast charging lithium-ion batteries: beyond material innovations, *J. Phys. D: Appl. Phys.*, 2025, **58**(25), 253001.
18 Y. Gu, *et al.*, A multifunctional NaxBi/NaCl flexible interface layer for solid-state Na metal batteries, *Adv. Funct. Mater.*, 2025, **35**(9), 2416077.
19 X. Xia, *et al.*, A Multifunctional Interphase Layer Enabling Superior Sodium-Metal Batteries under Ambient Temperature and– 40° C, *Adv. Mater.*, 2023, **35**(11), 2209511.
20 M. Ali, *et al.*, A multifunctional ex-situ artificial hybrid interphase layer to stabilize sodium metal anode, *Nano Energy*, 2024, **132**, 110348.
21 X. Wang, *et al.*, Addressing the low solubility of a solid electrolyte interphase stabilizer in an electrolyte by composite battery anode design, *ACS Appl. Mater. Interfaces*, 2021, **13**(11), 13354–13361.
22 P. Shi, *et al.*, Red phosphorous-derived protective layers with high ionic conductivity and mechanical strength on dendrite-free sodium and potassium metal anodes, *Adv. Energy Mater.*, 2021, **11**(5), 2003381.
23 D. Li, *et al.*, Rational design of an artificial SEI: Alloy/solid electrolyte hybrid layer for a highly reversible Na and K metal anode, *ACS Nano*, 2022, **16**(10), 16966–16975.
24 L. Gao, *et al.*, The chemical evolution of solid electrolyte interface in sodium metal batteries, *Sci. Adv.*, 2022, **8**(6), eabm4606.
25 C. Bao, *et al.*, Solid electrolyte interphases on sodium metal anodes, *Adv. Funct. Mater.*, 2020, **30**(52), 2004891.
26 Y. Zhong, *et al.*, Mechanistic insights into fast charging and discharging of the sodium metal battery anode: A comparison with lithium, *J. Am. Chem. Soc.*, 2021, **143**(34), 13929–13936.
27 T. Ortmann, *et al.*, Kinetics and pore formation of the sodium metal anode on NASICON-type Na3. 4Zr2Si2. 4P0. 6O12 for sodium solid-state batteries, *Adv. Energy Mater.*, 2023, **13**(5), 2202712.
28 P. Bai, *et al.*, Transition of lithium growth mechanisms in liquid electrolytes, *Energy Environ. Sci.*, 2016, **9**(10), 3221–3229.
29 X. Zheng, *et al.*, Knocking down the kinetic barriers towards fast-charging and low-temperature sodium metal batteries, *Energy Environ. Sci.*, 2021, **14**(9), 4936–4947.
30 D. Yu, *et al.*, Low-temperature and fast-charge sodium metal batteries, *Small*, 2024, **20**(30), 2311810.
31 Z. Tian, *et al.*, Electrolyte solvation structure design for sodium ion batteries, *Adv. Sci.*, 2022, **9**(22), 2201207.
32 Z. Lu, *et al.*, Step-by-step desolvation enables high-rate and ultra-stable sodium storage in hard carbon anodes, *Proc. Natl. Acad. Sci. U. S. A.*, 2022, **119**(40), e2210203119.
33 J. Qian, *et al.*, High rate and stable cycling of lithium metal anode, *Nat. Commun.*, 2015, **6**(1), 6362.
34 H. Wang, *et al.*, Ultrahigh–current density anodes with interconnected Li metal reservoir through overlithiation of mesoporous AlF3 framework, *Sci. Adv.*, 2017, **3**(9), e1701301.
35 M. Ali, *et al.*, Recent development in sodium metal batteries: challenges, progress, and perspective, *Mater. Today*, 2025, **88**, 730–751.
36 J. Zhang, *et al.*, Research progress of organic liquid electrolyte for sodium ion battery, *Front. Chem.*, 2023, **11**, 1253959.

37 Y. Pan, *et al.*, Investigation of the solid electrolyte interphase on hard carbon electrode for sodium ion batteries, *J. Electroanal. Chem.*, 2017, **799**, 181–186.
38 J. Fondard, *et al.*, SEI composition on hard carbon in Na-ion batteries after long cycling: influence of salts (NaPF6, NaTFSI) and additives (FEC, DMCF), *J. Electrochem. Soc.*, 2020, **167**(7), 070526.
39 Q. Zhao, S. Stalin and L. A. Archer, Stabilizing metal battery anodes through the design of solid electrolyte interphases, *Joule*, 2021, **5**(5), 1119–1142.
40 B. Han, *et al.*, Probing the Na metal solid electrolyte interphase via cryo-transmission electron microscopy, *Nat. Commun.*, 2021, **12**(1), 3066.
41 K. Li, *et al.*, Evolution of the electrochemical interface in sodium ion batteries with ether electrolytes, *Nat. Commun.*, 2019, **10**(1), 725.
42 M. Moorthy, *et al.*, Recent trends in artificial SEI layers for controlling dendrite formation and enhancing cycle life: toward stable and durable sodium metal batteries, *Small*, 2025, **21**(34), 2502974.
43 P. G. Kitz, *et al.*, Operando EQCM-D with simultaneous in situ EIS: new insights into interphase formation in Li ion batteries, *Anal. Chem.*, 2018, **91**(3), 2296–2303.
44 Y. Ji, *et al.*, In situ probing the origin of interfacial instability of Na metal anode, *Chem*, 2023, **9**(10), 2943–2955.
45 J. Seok, *et al.*, Visualization of sodium metal anodes via operando X-ray and optical microscopy: controlling the morphological evolution of sodium metal plating, *ACS Appl. Mater. Interfaces*, 2022, **14**(8), 10438–10446.
46 K. Lim, *et al.*, Porosity of solid electrolyte interphases on alkali metal electrodes with liquid electrolytes, *ACS Appl. Mater. Interfaces*, 2021, **13**(43), 51767–51774.
47 C. D. Fincher, *et al.*, Elastic and plastic characteristics of sodium metal, *ACS Appl. Energy Mater.*, 2020, **3**(2), 1759–1767.
48 M. J. Wang, *et al.*, Analysis of elastic, plastic, and creep properties of sodium metal and implications for solid-state batteries, *Materialia*, 2020, **12**, 100792.
49 W. S. LePage, *et al.*, Sodium mechanics: effects of temperature, strain rate, and grain rotation and implications for sodium metal batteries, *Extreme Mech. Lett.*, 2022, **52**, 101644.
50 D. A. Cogswell, Quantitative phase-field modeling of dendritic electrodeposition, *Phys. Rev. E:Stat., Nonlinear, Soft Matter Phys.*, 2015, **92**(1), 011301.
51 L. Chen, *et al.*, Modulation of dendritic patterns during electrodeposition: A nonlinear phase-field model, *J. Power Sources*, 2015, **300**, 376–385.
52 C. P. Nielsen and H. Bruus, Morphological instability during steady electrodeposition at overlimiting currents, *Phys. Rev. E:Stat., Nonlinear, Soft Matter Phys.*, 2015, **92**(5), 052310.
53 M. Z. Bazant, Theory of chemical kinetics and charge transfer based on nonequilibrium thermodynamics, *Acc. Chem. Res.*, 2013, **46**(5), 1144–1160.
54 J.-N. Chazalviel, Electrochemical aspects of the generation of ramified metallic electrodeposits, *Phys. Rev. A: At., Mol., Opt. Phys.*, 1990, **42**(12), 7355.
55 F. Shi, *et al.*, Lithium metal stripping beneath the solid electrolyte interphase, *Proc. Natl. Acad. Sci. U. S. A.*, 2018, **115**(34), 8529–8534.
56 J. Kasemchainan, *et al.*, Critical stripping current leads to dendrite formation on plating in lithium anode solid electrolyte cells, *Nat. Mater.*, 2019, **18**(10), 1105–1111.
57 D. Spencer Jolly, *et al.*, Sodium/Na β ″alumina interface: effect of pressure on voids, *ACS Appl. Mater. Interfaces*, 2019, **12**(1), 678–685.
58 D. Landmann, *et al.*, Sodium plating and stripping from Na-β″-alumina ceramics beyond 1000 mA/cm2, *Mater. Today Energy*, 2020, **18**, 100515.
59 M. Werres, *et al.*, Origin of heterogeneous stripping of lithium in liquid electrolytes, *ACS Nano*, 2023, **17**(11), 10218–10228.
60 L. Zhang, *et al.*, Unraveling gas evolution in sodium batteries by online electrochemical mass spectrometry, *Energy Storage Mater.*, 2021, **42**, 12–21.
61 X. Chen, *et al.*, Ion–solvent complexes promote gas evolution from electrolytes on a sodium metal anode, *Angew. Chem., Int. Ed.*, 2018, **57**(3), 734–737.
62 B. Michalak, *et al.*, Gas evolution in operating lithium-ion batteries studied in situ by neutron imaging, *Sci. Rep.*, 2015, **5**(1), 15627.
63 X. Li, *et al.*, Mechanisms and Mitigation Strategies of Gas Generation in Sodium-Ion Batteries, *Nano-Micro Lett.*, 2025, **17**(1), 177.
64 D. B. Thornton, *et al.*, Probing Degradation in Lithium Ion Batteries with On-Chip Electrochemistry Mass Spectrometry, *Angew. Chem.*, 2024, **136**(6), e202315357.
65 C. Gong, *et al.*, The role of an elastic interphase in suppressing gas evolution and promoting uniform electroplating in sodium metal anodes, *Energy Environ. Sci.*, 2023, **16**(2), 535–545.
66 X. Zhao, H. Ren and L. Luo, Gas bubbles in electrochemical gas evolution reactions, *Langmuir*, 2019, **35**(16), 5392–5408.
67 Y. Xiang, *et al.*, Gas induced formation of inactive Li in rechargeable lithium metal batteries, *Nat. Commun.*, 2023, **14**(1), 177.
68 E. W. C. Spotte-Smith, *et al.*, Elementary decomposition mechanisms of lithium hexafluorophosphate in battery electrolytes and interphases, *ACS Energy Lett.*, 2022, **8**(1), 347–355.
69 A. Tomaszewska, *et al.*, Lithium-ion battery fast charging: A review, *eTransportation*, 2019, **1**, 100011.
70 B. L. Rinkel, *et al.*, Electrolyte oxidation pathways in lithium-ion batteries, *J. Am. Chem. Soc.*, 2020, **142**(35), 15058–15074.
71 Z. Zhang, *et al.*, The influence of cathode degradation products on the anode interface in lithium-ion batteries, *ACS Nano*, 2024, **18**(13), 9389–9402.
72 Y. Gao, *et al.*, Low-Temperature and Fast-Charging Sodium Metal Batteries Enabled by Molecular Structure Regulation of Fluorinated Solvents, *Adv. Funct. Mater.*, 2025, **35**(5), 2414652.
73 B. L. Rinkel, *et al.*, Two electrolyte decomposition pathways at nickel-rich cathode surfaces in lithium-ion batteries, *Energy Environ. Sci.*, 2022, **15**(8), 3416–3438.

74 X. Wang, *et al.*, Building stable anodes for high-rate Na-metal batteries, *Adv. Mater.*, 2024, **36**(16), 2311256.
75 E. W. C. Spotte-Smith, *et al.*, A critical analysis of chemical and electrochemical oxidation mechanisms in Li-ion batteries, *J. Phys. Chem. Lett.*, 2024, **15**(2), 391–400.
76 J. Shin and M. Pharr, Fracture behavior of metallic sodium and implications for battery applications, *Mater. Horiz.*, 2022, **9**(12), 3102–3109.
77 Q. Lu, *et al.*, A facile method to stabilize sodium metal anodes towards high-performance sodium batteries, *J. Mater. Chem. A*, 2021, **9**(14), 9038–9047.
78 J.-P. Niemelä, *et al.*, Molecular layer deposited alucone thin films from long-chain organic precursors: from brittle to ductile mechanical characteristics, *Dalton Trans.*, 2020, **49**(31), 10832–10838.
79 Y. Zhao, K. Zheng and X. Sun, Addressing interfacial issues in liquid-based and solid-state batteries by atomic and molecular layer deposition, *Joule*, 2018, **2**(12), 2583–2604.
80 X. Xia, *et al.*, Rational design of a hybrid artificial protective layer for a dendrite-free, long-cycling-life Na metal anode, *Next Mater.*, 2024, **5**, 100245.
81 Z. Luo, *et al.*, Robust artificial interlayer for columnar sodium metal anode, *Nano Energy*, 2022, **97**, 107203.
82 Q. Lu, *et al.*, Recent advances in stabilization of sodium metal anode in contact with organic liquid and solid-state electrolytes, *Energy Technol.*, 2022, **10**(7), 2200149.
83 S. Wenzel, *et al.*, Interfacial reactivity benchmarking of the sodium ion conductors Na3PS4 and sodium β-alumina for protected sodium metal anodes and sodium all-solid-state batteries, *ACS Appl. Mater. Interfaces*, 2016, **8**(41), 28216–28224.
84 M. Zhu, *et al.*, Dendrite-free sodium metal anodes enabled by a sodium benzenedithiolate-rich protection layer, *Angew. Chem.*, 2020, **132**(16), 6658–6662.
85 Z. Hou, *et al.*, Poly (vinylidene difluoride) coating on Cu current collector for high-performance Na metal anode, *Energy Storage Mater.*, 2020, **24**, 588–593.
86 C. Wang, *et al.*, Robust Anode-Free Sodium Metal Batteries Enabled by Artificial Sodium Formate Interface, *Adv. Energy Mater.*, 2023, **13**(22), 2204125.
87 X. Li, *et al.*, An encapsulation-based sodium storage via Zn-single-atom implanted carbon nanotubes, *Adv. Mater.*, 2022, **34**(31), 2202898.
88 J. Qian, *et al.*, Protecting lithium/sodium metal anode with metal-organic framework based compact and robust shield, *Nano Energy*, 2019, **60**, 866–874.
89 M. E. Lee, *et al.*, Catalytic pyroprotein seed layers for sodium metal anodes, *ACS Appl. Mater. Interfaces*, 2019, **11**(13), 12401–12407.
90 Z. Wang, *et al.*, Conducting polymer paper-derived mesoporous 3D N-doped carbon current collectors for Na and Li metal anodes: A combined experimental and theoretical study, *J. Phys. Chem. C*, 2018, **122**(41), 23352–23363.
91 X. Lv, *et al.*, Construction of inorganic/organic hybrid layer for stable Na metal anode operated under wide temperatures, *Small*, 2023, **19**(30), 2300215.
92 P. Pirayesh, *et al.*, From Nanoalloy to Nano-Laminated Interfaces for Highly Stable Alkali-Metal Anodes, *Adv. Mater.*, 2023, **35**(29), 2301414.
93 P. Liu, *et al.*, Inorganic–organic hybrid multifunctional solid electrolyte interphase layers for dendrite-free sodium metal anodes, *Angew. Chem., Int. Ed.*, 2023, **62**(47), e202312413.
94 S. Wu, *et al.*, Practical level of low-N/P ratio sodium metal batteries: On the basis of deposition/dissolution efficiency in the aspects of electrolytes and temperature, *Energy Storage Mater.*, 2023, **61**, 102897.